

# Statistics of the excursion sets in models with local primordial non-Gaussianity

Graziano Rossi<sup>1\*</sup>, Pravabati Chingangbam<sup>1,2†</sup> and Changbom Park<sup>1‡</sup>

<sup>1</sup> *Korea Institute for Advanced Study, Hoegiro 87, Dongdaemun-Gu, Seoul 130 – 722, South Korea*

<sup>2</sup> *Astrophysical Research Center for the Structure and Evolution of the Cosmos, Sejong University, 98 Gunja Dong, Gwangjin gu, Seoul 143747, South Korea*

31 October 2018

## ABSTRACT

We use the statistics of regions above or below a temperature threshold (excursion sets) to study the cosmic microwave background (CMB) anisotropy in models with primordial non-Gaussianity of the local type. By computing the full-sky spatial distribution and clustering of pixels above/below threshold from a large set of simulated maps with different levels of non-Gaussianity, we find that a positive value of the dimensionless non-linearity parameter  $f_{\text{NL}}$  enhances the number density of the cold CMB excursion sets along with their clustering strength, and reduces that of the hot ones. We quantify the robustness of this effect, which may be important to discriminate between the simpler Gaussian hypothesis and non-Gaussian scenarios, arising either from non-standard inflation or alternative early-universe models. The clustering of hot and cold pixels exhibits distinct non-Gaussian signatures, particularly at angular scales of about 75 arcmin (i.e. around the Doppler peak), which increase linearly with  $f_{\text{NL}}$ . Moreover, the clustering changes strongly as a function of the smoothing angle. We propose several statistical tests to maximize the detection of a local primordial non-Gaussian signal, and provide some theoretical insights within this framework, including an optimal selection of the threshold level. We also describe a procedure which aims at minimizing the cosmic variance effect, the main limit within this statistical framework.

**Key words:** methods: statistical – cosmic microwave background, correlations — cosmology: observations.

## 1 INTRODUCTION

Since some level of non-Gaussianity is generically expected in all inflation models, due to interactions of the inflaton with gravity and/or from inflaton self-interactions, seeking for deviations from the Gaussian paradigm has recently become a major effort – and a minor industry – in cosmology. Properties of the primordial perturbations are uniquely imprinted in the cosmic microwave background (CMB) anisotropy distribution; hence, its analysis is a powerful way of looking at the specifics of the inflationary models (or alternatives to inflation). At the present time, the main challenge is either to detect or to constrain mild or weak departures from primordial Gaussian initial conditions, as the level of non-Gaussianity predicted in the simplest single-field

slow-roll inflation is slightly below the minimum value detectable by the Planck satellite, and not within reach of future galaxy surveys. This is essentially why primordial non-Gaussianity is regarded as one of the most promising probes of the inflationary universe (Komatsu et al. 2009b), and it has received a recent boost, both theoretically and observationally, mainly because of the *Wilkinson Microwave Anisotropy Probe* (WMAP) data which seems to favor a slightly positive value of the dimensionless non-linearity parameter  $f_{\text{NL}}$  (Yadav & Wandelt 2008; Komatsu et al. 2009a, 2010; Smith et al. 2009).

From the theoretical side, much effort has been directed towards the development of competing scenarios for perturbation generation which go beyond the single-field slow-roll paradigm, for instance by the inclusion in the Lagrangian of non-trivial kinetic terms, the presence of more than one light field during inflation, the temporary violation of slow-roll, or a non-adiabatic initial vacuum state for the inflaton.

\* Email: graziano@kias.re.kr

† Email: prava@kias.re.kr

‡ Email: cbp@kias.re.kr

Examples are the curvaton model, the modulated reheating, DBI or ghost inflation, or multi-field scenarios, some of which imply large departures from Gaussianity (see, for instance, among the plethora of papers on this subject, Linde & Mukhanov 1997; Lyth & Wands 2002; Acquaviva et al. 2003; Lyth, Ungarelli & Wands 2003; Maldacena 2003; Alshahiha et al. 2004; Arkani-Hamed et al. 2004; Bartolo et al. 2004; Dvali, Gruzinov & Zaldarriaga 2004; Chen 2005; Seery & Lidsey 2005; Bartolo, Matarrese & Riotto 2006; Lyth & Riotto 2006; Sasaki et al. 2006; Creminelli et al. 2007; Creminelli & Senatore 2007; Koyama et al. 2007; Buchbinder et al. 2008; Chen et al. 2008, 2009; Lehnert & Steinhardt 2008; Matarrese & Verde 2008; Sasaki 2008; Bartolo & Riotto 2009; Brandenberger 2009; Naruko & Sasaki 2009; Senatore, Tashev & Zaldarriaga 2009; Silvestri & Trodden 2009; Bartolo, Matarrese & Riotto 2010).

From the observational point of view, the main goal is to constrain the level of primordial non-Gaussianity directly from a real data set, and this is usually achieved by constructing and applying a variety of non-Gaussian estimators such as the 3-point function (Hinshaw et al. 1994; Gangui et al. 1994), the genus statistics or the topological genus density (Coles 1988; Gott et al. 1990; Smoot et al. 1994; Colley & Gott 2003; Park 2004; Gott et al. 2007), the other Minkowski functionals (Schmalzing & Gorski 1998; Winitzki & Kosowsky 1998; Banday, Zaroubi & Gorski 2000; Hikage et al. 2006, 2008b; Matsubara 2010), the bispectrum and trispectrum (Spergel et al. 2007; Komatsu et al. 2009; Rudjord et al. 2009; Liguori et al. 2010), tensor modes (Coulson, Crittenden & Turok 1994), wavelets (Cabella et al. 2005; Curto et al. 2009; Vielva & Sanz 2009), pixel and peak statistics (Adler 1981; Bond & Efstathiou 1987; Coles and Barrow 1987; Kogut et al. 1995, 1996; Barreiro et al. 1997, 1998; Heavens 1998; Heavens & Sheth 1999; Heavens & Gupta 2001; Hernández-Monteagudo et al. 2004; Rossi et al. 2009; Hou et al. 2010), phase correlations, multifractals, and so forth (see also Komatsu, Spergel & Wandelt 2005; Chen & Szapudi 2006; Munshi & Heavens 2010). In this process, many observational challenges and experimental artifacts come into play; therefore, it is perhaps not surprising that controversial results and a long list of anomalies have been reported so far, ranging from a low value of the quadrupole till North-South or parity asymmetries, strange alignments in the data, and much more (see for example Chiang et al. 2003, 2007; Tegmark et al. 2003; de Oliveira-Costa et al. 2004; Eriksen et al. 2004, 2007; Schwarz et al. 2004; Cruz et al. 2005, 2006, 2007, 2008; Land & Magueijo 2005, 2007; Naselsky et al. 2005; Copi et al. 2006, 2007; Vielva et al. 2007; Gurzadyan et al. 2008; Pietroniro et al. 2009; Räth et al. 2009; Kim & Naselsky 2010).

Deviations from Gaussian initial conditions (if any) also carry important consequences on many aspects of the large-scale structure (LSS) of the Universe, and galaxy surveys can provide constraints on non-Gaussianity competitive with those from the CMB alone. There are in fact modifications in the statistics of voids (Kamionkowski, Verde & Jimenez 2009), in the distribution of neutral hydrogen and in the intergalactic medium (Viel et al. 2009), in the high-mass tail of the halo distribution (Chiu et al. 1998; Matarrese, Verde & Jimenez 2000; Sefusatti & Komatsu 2007; LoVerde et al. 2008), in the large-scale skewness of the galaxy distribution (Chodorowski & Bouchet 1996), in the number counts of

clusters and of density peaks (Desjacques et al. 2009; Jeong & Komatsu 2009), in the measurement of the scale dependence of the bias of LSS tracers (Carbone et al. 2008; Dalal et al. 2008; Verde & Matarrese 2009; Desjacques & Seljak 2010), in the reionization history (Crociani et al. 2009), in the galaxy power spectrum and bispectrum (Scoccimarro 2000; Scoccimarro et al. 2004; Mangilli & Verde 2009), in the topology (Park et al. 1998, 2005; Gott et al. 2008; Hikage et al. 2008a), and in the abundance and clustering of galaxies and dark matter halos (Verde et al. 2001; Afshordi & Tolley 2008; Grossi et al. 2008; LoVerde et al. 2008; Matarrese & Verde 2008; McDonald 2008; Slosar et al. 2008; Taruya et al. 2008; Pillepich et al. 2010).

Despite all these remarkable theoretical and observational efforts, till date the experimental detection of a significant deviation from the Gaussian paradigm remains still challenging and not convincing. In this respect, we need to explore alternative statistics more sensitive to deviations from Gaussianity, and to search for unique features which may allow one to distinguish among the myriad of inflation models available in the literature. It is important to adopt different and complementary statistical approaches, and not just a single view, because non-Gaussianity can take innumerable forms. In fact, while Gaussian random processes are theoretically desirable since they are the only ones for which the knowledge of all spectral parameters completely determines all the statistical properties, as soon as we introduce departures from Gaussianity a more complicated scenario emerges, and there is no such statistics which describes fully and uniquely the non-Gaussian nature of a sample. In particular, moving away from standard estimators like the bispectrum, trispectrum, three and four-point functions, skewness, etc, we are interested here in rare events, which can often maximize deviations from what is predicted by a Gaussian distribution.

The main goal of the present work is to extend and apply the statistics of the excursion sets, regions above or below a temperature threshold, to models with primordial non-Gaussianity. Specifically, we focus on the *local* parametrization of non-Gaussianity (Salopek & Bond 1990), by including quadratic corrections to the curvature perturbation. We simulate a large set of full-sky maps with different  $f_{\text{NL}}$  values, and compute the number density and the spatial clustering of the CMB excursion set regions. We also provide the theoretical formalism to interpret our results. The excursion set statistics is fully characterized in the context of Gaussian random fields (Kaiser 1984; Bardeen et al. 1986), and it has been used in a variety of studies (see for example Jensen & Szalay 1986; Bond & Efstathiou 1987; Barreiro et al. 2001; Kashlinsky et al. 2001 and references therein). There are also some extensions to non-Gaussian conditions in the literature (i.e. Coles & Barrow 1987; Coles 1988; Barreiro et al. 1998). Our analysis differs from those of the previous authors primarily because we use a more realistic model for non-Gaussianity supported by  $f_{\text{NL}}$  type simulations, and because we also propose some new statistical tools, tests, and theoretical insights within this framework. In particular, while in precedent studies it has always been shown that the Gaussian correlation function of the excursion sets and peaks (a subset of the excursion sets) is easily distinguishable from a non-Gaussian one, even if the underlying bispectra are not statistically different (i.e. Kogut et

al. 1995; Barreiro et al. 1998; Heavens & Gupta 2001), we suggest here that it may not be the case if the model of non-Gaussianity is of the local type, and the resolution adopted is not optimal.

Our work is also motivated by another reason. In a previous analysis (Rossi et al. 2009), we compared the pixel clustering statistics – properly extended to handle inhomogeneous noise – against WMAP five-year data, and we detected deviations from the Gaussian theoretical expectations. In particular, we found a remarkable difference in the clustering of hot and cold pixels at relatively small angular scales. A similar trend has also been reported in the literature by Tojeiro et al. (2006), and by Hou, Banday & Gorski (2010), although at much larger scales. Whether or not this discrepancy may arise from primordial non-Gaussianity of the local type is another key question of this analysis.

The layout of the paper is as follows. Section 2 contains the theoretical tools developed and used in this study. In Section 2.1 we briefly describe the local  $f_{\text{NL}}$  model. In Section 2.2 we explain how the simulated non-Gaussian maps are constructed. In Section 2.3 we provide the basic formalism for the excursion sets statistics, in the context of  $f_{\text{NL}}$  scenarios. Expressions for the one- and two-dimensional probability distribution functions (PDFs) are given, under the assumption of weak non-Gaussianity; this is done via a perturbative approach by the multidimensional Edgeworth expansion around a Gaussian distribution function. Those PDFs are then used to characterize the number density and the clustering statistics above/below threshold as a function of  $f_{\text{NL}}$  (some details are provided in Appendix A). In Section 2.4 we relate the excursion sets formalism to other commonly used topological estimators. In Section 3, computations of the number density and the clustering statistics above/below threshold from non-Gaussian maps are presented and interpreted according to our theory predictions. Specifically, Section 3.1 shows the abundance of the excursion set regions in a variety of ways, while in Section 3.2 we highlight some statistical tests developed using the number density. We also argue that there are optimal thresholds which can maximize the non-Gaussian contribution, as well as levels which do not allow to distinguish a Gaussian signal from a non-Gaussian one. In Section 3.3 we present the clustering of hot and cold pixels for one of the optimal temperature thresholds as a function of the smoothing scale, and in Section 3.4 we propose a new statistical test derived from the clustering statistics. This procedure aims at minimizing the cosmic variance effect, and involves the computation of the power spectrum for any given CMB map. A final part (Section 4) summarizes our findings, and highlights ongoing and future work. We leave in Appendix B, C and D some technical details regarding experimental artifacts such as inhomogeneous noise, incomplete sky coverage, errorbar estimates and confusion effects caused by spurious non-Gaussianities; all these experimental complications will be examined in more detail in the forthcoming publications.

## 2 THEORETICAL FRAMEWORK

In this paper we study the statistics of the excursion sets in CMB temperature maps, to examine its sensitivity to primordial non-Gaussianity. Even though the chosen statistics

should be sensitive to a wide class of non-Gaussian fields, in the present work we consider the local  $f_{\text{NL}}$  model in detail.

### 2.1 The local $f_{\text{NL}}$ model

Considerable interest has been recently focused on local type  $f_{\text{NL}}$ , by which the non-Gaussianity of Bardeen’s curvature perturbations is *locally* characterized in real space, up to second order, by:

$$\Phi(\mathbf{x}) = \phi(\mathbf{x}) + f_{\text{NL}}[\phi^2(\mathbf{x}) - \langle \phi^2 \rangle] \quad (1)$$

and in Fourier space by

$$\Phi(\mathbf{k}) = \phi(\mathbf{k}) + f_{\text{NL}} \int \frac{d^3k'}{(2\pi)^3} \phi(\mathbf{k} + \mathbf{k}') \phi(\mathbf{k}'), \quad (2)$$

where  $\phi$  is a Gaussian field (Salopek & Bond 1990; Gangui et al. 1994; Verde et al. 2000; Komatsu & Spergel 2001). The local type non-Gaussianity is sensitive to the bispectrum  $B_{\Phi}(k_1, k_2, k_3)$  with squeezed configuration triangles (i.e.  $k_1 \ll k_2 \sim k_3$ ; Babich et al. 2004), defined as

$$\begin{aligned} \langle \Phi_{\mathbf{k}_1} \Phi_{\mathbf{k}_2} \Phi_{\mathbf{k}_3} \rangle &= \delta_{\text{D}}^3(\mathbf{k}_{123}) B_{\Phi}(k_1, k_2, k_3) \\ &= \delta_{\text{D}}^3(\mathbf{k}_{123}) f_{\text{NL}} F(k_1, k_2, k_3) \end{aligned} \quad (3)$$

where  $\delta_{\text{D}}$  is the Dirac delta,  $\mathbf{k}_{123} = \mathbf{k}_1 + \mathbf{k}_2 + \mathbf{k}_3$  and  $f_{\text{NL}}$  is a dimensionless parameter (or more generally a non-linearity function), while the function  $F$  describes the dependence on the shape of triangular configurations defined by the three wave-numbers  $k_1, k_2, k_3$ .

This parametrization was originally motivated by the single-field inflation scenarios, and it became quite popular shortly thereafter because it is possible to cast many inflationary models, including the curvaton scenario (Lyth et al. 2003), in the form of equation (3); namely, one can express departures from non-Gaussianity in terms of a generic function  $F$ , which may assume different model-dependent shapes and it is broadly classified into three classes (local squeezed, non-local equilateral, orthogonal), and the parameter or function  $f_{\text{NL}}$ . Alternatives to inflation like New Ekpyrotic and cyclic models are also expected to produce a large level of non-Gaussianity of this type (Koyama et al. 2007; Buchbinder et al. 2008; Lehnert & Steinhardt 2008). Therefore, the power of this formalism is that it allows one to rule out a large class of models by putting constraints on  $f_{\text{NL}}$ , and to reconstruct the inflationary action starting from a measurement of a few observables like  $f_{\text{NL}}$  itself.

Note that in this paper we always use  $f_{\text{NL}}$  in its local meaning, even if the usual superscript *local* is not present, and also that there are two distinct definitions of  $f_{\text{NL}}$  in the literature, corresponding to a CMB and a LSS convention. In the CMB convention adopted here, the local non-Gaussianity is defined by equations (1-3) with the curvature perturbations  $\Phi$  evaluated at early times during the matter domination era, when their value was constant. In the LSS convention, one usually assumes  $\Phi$  to be the value linearly extrapolated at present time, and therefore it includes the late-time effect of the accelerated expansion in a cold dark matter cosmology with a cosmological constant ( $\Lambda$ CDM).

Current limits on the primordial non-Gaussianity parameter  $f_{\text{NL}}$  at 95% confidence level (CL) from the CMB alone are claimed to be  $-4 < f_{\text{NL}} < 80$  (Smith et al. 2009),  $-18 < f_{\text{NL}} < 80$  (Curto et al. 2009),  $-36 < f_{\text{NL}} < 58$  (Smidt

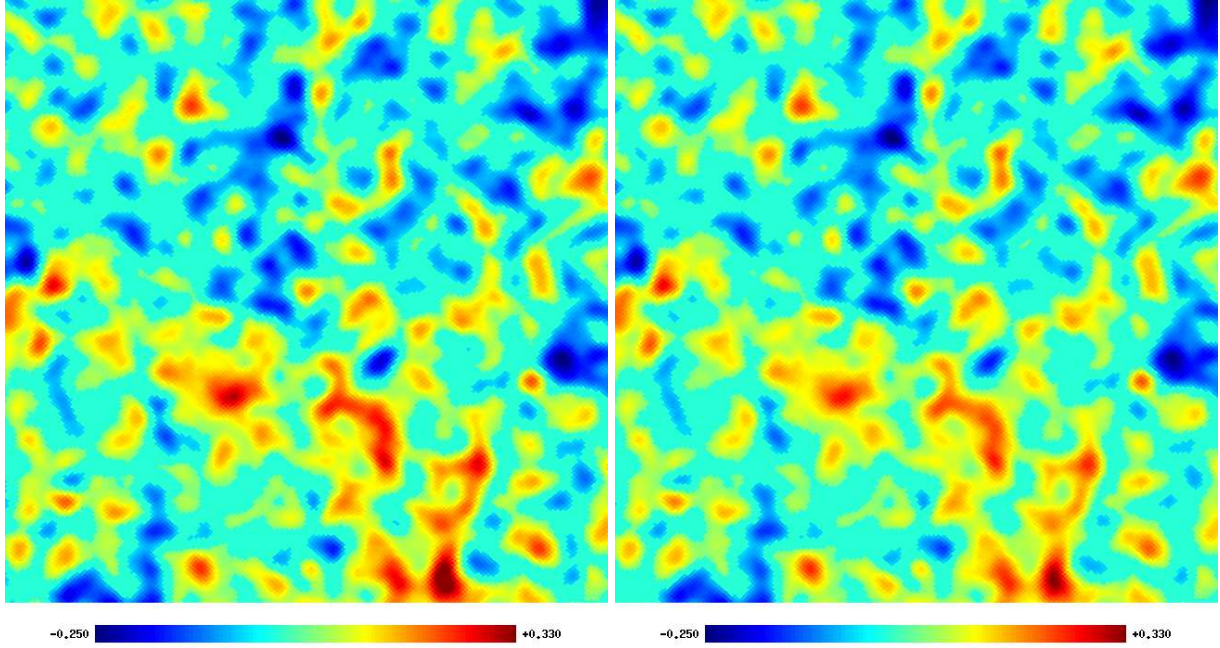


**Figure 1.** A small patch ( $\simeq 10^\circ \times 10^\circ$ ) of the simulated CMB sky with primordial Gaussianity (left panel) and non-Gaussianity of the local type with  $f_{\text{NL}} = 500$  (right panel), when smoothed with a Gaussian beam of FWHM=30 arcmin; regions below the threshold  $\nu = 0.50$  or above  $\nu = -0.50$  are set to zero. The temperature scale is in mK, ranging from -0.250 to +0.330.

et al. 2010), and  $-10 < f_{\text{NL}} < 74$  (Komatsu et al. 2010). Those obtained from the LSS are similarly competitive; see for instance  $-29 < f_{\text{NL}} < 70$  by Slosar et al. (2008).

## 2.2 Simulating non-Gaussian maps

The simulated non-Gaussian maps used in this analysis are constructed following the method outlined in Liguori et al (2003). The main point of their procedure is to calculate the spherical harmonic coefficients  $a_{\ell m}$ 's as an integral in real, rather than in Fourier space. Briefly, the CMB temperature fluctuations are expanded in terms of spherical harmonics as  $\delta T(\hat{n}) = \sum_{\ell m} a_{\ell m} Y_{\ell m}(\hat{n})$ . The  $a_{\ell m}$ 's are then computed by convolving the primordial potential fluctuations with the radiation transfer function  $\Delta_\ell$  (independently computed using CMBFAST developed by Seljak & Zaldarriaga 1996), as

$$\begin{aligned} a_{\ell m} &= 4\pi(-i)^\ell \int \frac{d^3 k}{(2\pi)^3} \Phi(\mathbf{k}) \Delta_\ell(k) Y_{\ell m}^*(\hat{\mathbf{k}}) \\ &= \frac{(-i)^\ell}{2\pi^2} \int dk k^2 \Phi_{\ell m}(k) \Delta_\ell(k) \\ &= \int dr r^2 \Phi_{\ell m}(r) \Delta_\ell(r) \end{aligned} \quad (4)$$

where

$$\begin{aligned} \Phi_{\ell m}(k) &= \int d\Omega_{\hat{\mathbf{k}}} \Phi(\mathbf{k}) Y_{\ell m}(\hat{\mathbf{k}}) \\ &= 4\pi(i)^\ell \int dr r^2 \Phi_{\ell m}(r) j_\ell(kr) \end{aligned} \quad (5)$$

$$\Phi_{\ell m}(r) = \frac{(-i)^\ell}{2\pi^2} \int dk k^2 \Phi_{\ell m}(k) j_\ell(kr) \quad (6)$$

$$\Delta_\ell(r) = \frac{2}{\pi} \int dk k^2 \Delta_\ell(k) j_\ell(kr). \quad (7)$$

$\Phi(\mathbf{k})$  is the Fourier transform of the real space potential  $\Phi(\mathbf{x})$  defined in equations (1) and (2),  $\Phi_{\ell m}(r)$  is the real space harmonic potential,  $\Phi_{\ell m}(k)$  is its inverse and  $j_\ell$ 's are spherical Bessel functions.

In presence of non-Gaussianity of the local type, from equations (1-6) and for a constant  $f_{\text{NL}}$  it follows immediately that

$$\Phi_{\ell m} = \Phi_{\ell m}^{\text{G}} + f_{\text{NL}} \Phi_{\ell m}^{\text{fNL}} \quad (8)$$

$$a_{\ell m} = a_{\ell m}^{\text{G}} + f_{\text{NL}} a_{\ell m}^{\text{fNL}}, \quad (9)$$

where in both equations the first right-hand side terms are the Gaussian contributions, while the second ones account for the  $f_{\text{NL}}$  part. Note that those terms are integrals over the corresponding potentials (i.e.  $\Phi_{\ell m}^{\text{G}}$  involves  $\phi$  only, while  $\Phi_{\ell m}^{\text{fNL}}$  accounts for  $\phi^2$  – see again equations 1 and 2). The Gaussian part in (8) is obtained in real space from

$$\Phi_{\ell m}^{\text{G}}(r) = \int dr' r'^2 n_{\ell m}(r') W_\ell(r, r') \quad (10)$$

where  $n_{\ell m}(r)$  are independent complex Gaussian variables,  $W_\ell(r, r')$  are filter functions defined by

$$W_\ell(r, r') = \frac{2}{\pi} \int dk k^2 \sqrt{P_\Phi(k)} j_\ell(kr) j_\ell(kr') \quad (11)$$

and obtained as in Chingangbam & Park (2009), and  $P_\Phi(k)$  is the primordial power spectrum adopted. After computing the Gaussian part of the potential  $\phi(\mathbf{x}) = \sum_{\ell m} \Phi_{\ell m}^{\text{G}}(r) Y_{\ell m}(\hat{r})$  it is straightforward to compute the corresponding  $f_{\text{NL}}$  contribution, and eventually the non-Gaussian temperature fluctuations via equations (4) and (9).

Our simulations are provided in the HEALPix scheme (Górski et al. 1999) at a resolution of  $N_{\text{side}} = 512$ , giving a total of 3145728 pixels separated on average by  $\theta_{\text{pix}} = 6.87$  arcmin. We adopt a standard LCDM cosmological model, with the WMAP 5-year best fit parameters (Komatsu et al. 2009). An example of these realizations is shown in Figure 1 for a small patch of the sky ( $\simeq 10^\circ \times 10^\circ$ ). Regions below a temperature threshold  $\nu = 0.50$  or above  $\nu = -0.50$  are set to zero, where  $\nu = \delta T/\sigma$ , with  $\sigma$  being the rms of the map and  $\delta T$  the temperature anisotropy. The left panel highlights the Gaussian case, the right panel shows the corresponding non-Gaussian scenario with  $f_{\text{NL}} = 500$ . A Gaussian smoothing with a full width at half-maximum (FWHM) of 30 arcmin is applied to those regions before clipping the field at  $\nu = \pm 0.50$ . Clearly, by visual inspection it is hard to distinguish between the two maps, although one can easily show that their underlying skewness is quite different.

### 2.3 Excursion sets formalism in $f_{\text{NL}}$ models

Given a CMB map with a temperature assigned to each point, an excursion set is the ensemble of all pixels with temperatures greater than a fixed threshold. The complementary excursion set for temperatures lesser than a given level is symmetrically defined; in the Gaussian case, it is expected to give the same results as the corresponding hot excursion set. If the threshold under consideration is high enough, the excursion set is composed of many disjoint groups of pixels, each group surrounding one of the local maxima or temperature peak (see Figure 1). The excursion set regions are easily and unambiguously identifiable in the CMB sky rather than the distributions of peaks, and at high thresholds the number of maxima and excursion sets coincides asymptotically. We are interested here in understanding how the number density and the clustering statistics of the excursion regions are modified in the presence of local, and relatively weak, non-Gaussianity. This theoretical framework will guide the interpretation of our numerical results presented in Section 3, from a large set of non-Gaussian simulations.

In a full Gaussian sky and in the absence of pixel noise, the number density of regions above (below) a temperature threshold  $\nu$  is simply given by:

$$n_{\text{pix}}^{\text{G}}(\nu) = \frac{N_{\text{pix,tot}}}{4\pi} \cdot \frac{\text{erfc}(\nu/\sqrt{2})}{2}, \quad (12)$$

where  $N_{\text{pix,tot}} = 12N_{\text{side}}^2$  is the total number of pixels in the map, at a resolution specified by the parameter  $N_{\text{side}}$ . Equation (12) follows immediately from an integration above (below) a level  $\nu$  of a one-dimensional Gaussian PDF.

In presence of non-Gaussianity of the local  $f_{\text{NL}}$  type, the theoretical formalism for the number density is complicated by the inclusion of an extra term which quantifies the role of  $f_{\text{NL}}$ . Following Matsubara (1994, 2003) and Hikage, Komatsu & Matsubara (2006), for weak non-Gaussianity a perturbative approach by the multidimensional Edgeworth expansion around a Gaussian distribution function suggests that the expression for the number density will acquire an additional term:

$$n_{\text{pix}}^{\text{NG}}(\nu) = n_{\text{pix}}^{\text{G}}(\nu) + n_{\text{pix}}^{\text{fNL}}(\nu) \quad (13)$$

where

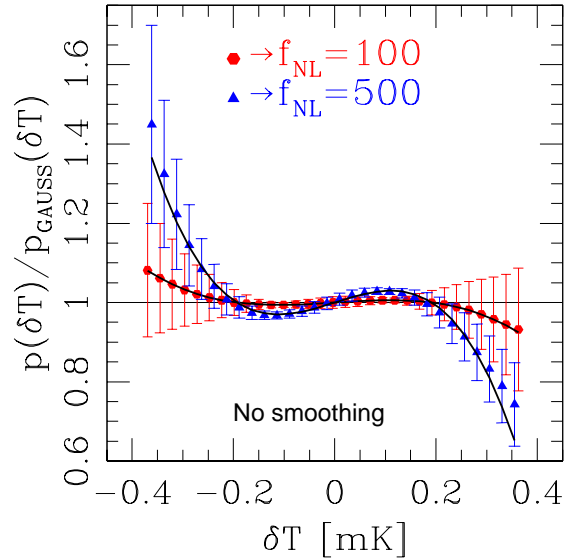


**Figure 2.** CMB temperature distribution (mK units) in presence of weak local non-Gaussianity, when no smoothing is applied. Points in the figure are averages over 200 non-Gaussian simulations with  $f_{\text{NL}} = 100$  and 500, errorbars are the corresponding  $1\sigma$  run-to-run estimates, and solid lines are from equation (15) for the two different  $f_{\text{NL}}$  values. The average rms of  $\delta T$  is 0.111 mK.

$$n_{\text{pix}}^{\text{fNL}}(\nu) = \frac{N_{\text{pix,tot}}}{4\pi} \left\{ \frac{\sigma S^{(0)}}{6\sqrt{2\pi}} (\nu^2 - 1) e^{-\nu^2/2} \right\}. \quad (14)$$

The skewness parameter  $S^{(0)} \equiv \langle \delta T^3 \rangle / \sigma^4$  needs to be evaluated numerically; it contains the reduced bispectrum specific to the non-Gaussian model – simplified for  $f_{\text{NL}}$  constant, as given by Komatsu & Spergel (2001). Note that  $S^{(0)}$  is an important parameter because it represents the leading order contribution to the non-Gaussianity. In fact  $\sigma S^{(0)} = f_{\text{NL}} \cdot A(\theta_s)$ , with  $A(\theta_s)$  a numerical coefficient which depends on the adopted smoothing  $\theta_s$ .

This implies that the underlying one-dimensional PDF in presence of local non-Gaussianity is given by:

$$p(\mu)d\mu \approx \frac{1}{\sqrt{2\pi}} e^{-\mu^2/2} \left\{ 1 + \frac{\sigma S^{(0)}}{6} \mu(\mu^2 - 3) \right\} d\mu, \quad (15)$$

where the first part on the right hand side of the equation is the usual Gaussian contribution, the second is the non-Gaussian term, and  $\mu = \delta T/\sigma$  is now used to indicate the threshold level. A plot of this distribution in units of the corresponding Gaussian PDF is provided in Figure 2, for  $f_{\text{NL}} = 100$  and 500, when no smoothing is applied. Points in the figure are averages over 200 realizations, errorbars are the  $1\sigma$  run-to-run estimates from the simulations, and solid lines are from equation (15). Note that, although the non-Gaussian term in (15) is complicated by the inclusion of  $S^{(0)}$ ,  $S^{(0)}$  itself is independent of the threshold level; this will be important for the next considerations.

With the one-dimensional PDF at hand, a number of well-known properties in the context of Gaussian random fields, such as the mean size and frequency of occurrence of the excursion sets above a given level (Coles & Barrow 1987; Kogut et al. 1995), can be easily generalized to  $f_{\text{NL}}$  models.

We will present this analysis in a following paper, while here we focus primarily on the pixel clustering statistics.

The correlation of the excursion sets above a threshold  $\nu$  is given by (Kaiser 1984):

$$1 + \xi_\nu(\theta) = P_2/P_1^2 \quad (16)$$

where

$$P_1 = \int_\nu^\infty p(\mu) d\mu \quad (17)$$

and

$$P_2 = \int_\nu^\infty d\mu_1 \int_\nu^\infty d\mu_2 p(\mu_1, \mu_2, w) \quad (18)$$

with  $p(\mu_1, \mu_2, w)$  being the two-dimensional PDF and  $w \equiv w(\theta) = \langle \mu_1 \mu_2 \rangle$  the correlation.

There have been attempts in the literature to generalize equation (16) to non-Gaussian cases. For example, Berry (1973), Jones (1996) and Barreiro et al. (1998) write  $p(\mu_1, \mu_2, w)$  as:

$$p(\mu_1, \mu_2, w) = p(\mu_1) \delta_D(\mu_1 - \mu_2) w + p(\mu_1) p(\mu_2) (1 - w) \quad (19)$$

so that (16) is simply given by:

$$1 + \xi_\nu(\theta) = w/P_1 + (1 - w). \quad (20)$$

Expression (20) implies that one can fully characterize the clustering statistics above (below) threshold using only the knowledge of the one-dimensional PDF (15) and the correlation. Unfortunately, this toy model cannot be applied in our context; equation (20) is valid when  $w$  is small, which is not true in our case.

Instead, since we are interested in weak non-Gaussianity, we expect a bivariate Edgeworth expansion to provide a reasonably good description at low thresholds:

$$p(\mu_1, \mu_2, w) d\mu_1 d\mu_2 \approx \frac{1}{2\pi\sqrt{1-w^2}} \exp\left\{-\frac{\mu_1^2 + \mu_2^2 - 2\mu_1\mu_2 w}{2(1-w^2)}\right\} \times \left[1 + \sigma S^{(0)}\left(\frac{H_{30} + H_{03}}{6}\right) + \lambda\left(\frac{H_{21} + H_{12}}{2}\right)\right] d\mu_1 d\mu_2 \quad (21)$$

where  $\lambda = \langle \mu_1^2 \mu_2 \rangle \equiv \langle \mu_1 \mu_2^2 \rangle$  and

$$\begin{aligned} H_{30}(\mu_1, \mu_2, w) &= H_{03}(\mu_2, \mu_1, w) \\ &= \frac{(\mu_1 - w\mu_2)^3}{(1-w^2)^3} - \frac{3(\mu_1 - w\mu_2)}{(1-w^2)^2} \end{aligned} \quad (22)$$

$$\begin{aligned} H_{21}(\mu_1, \mu_2, w) &= H_{12}(\mu_2, \mu_1, w) \\ &= \frac{2w(\mu_1 - w\mu_2) - (\mu_2 - w\mu_1)}{(1-w^2)^2} \\ &\quad + \frac{(\mu_2 - w\mu_1)(\mu_1 - w\mu_2)^2}{(1-w^2)^3}. \end{aligned} \quad (23)$$

Equation (21) is the two-dimensional version of the distribution (15) – see also Kotz, Balakrishnan & Johnson (2000) and Lam & Sheth (2009). Note that  $w$  and  $\lambda$  must be evaluated numerically. By inserting (15) and (21) into (16), it is possible to characterize the clustering strength of pixels above/below threshold for weak non-Gaussianity.

When  $f_{\text{NL}} = 0$  (i.e. in the Gaussian limit) equation (21) reduces to the usual bivariate Gaussian distribution, since  $\sigma S^{(0)} \equiv 0$  and  $\lambda \equiv 0$ . Therefore (16) reduces to the well-known formula:

$$1 + \xi_\nu(\theta) \rightarrow 1 + \xi_\nu^G(\theta)$$

$$\equiv \frac{\sqrt{2/\pi}}{\text{erfc}^2(\nu/\sqrt{2})} \int_\nu^\infty d\mu e^{-\mu^2/2} \text{erfc}\left[\frac{\nu - w\mu}{\sqrt{2(1-w^2)}}\right] \quad (24)$$

where

$$w \equiv w(\theta) = \langle \delta T_1 \delta T_2 \rangle / \sigma^2 \rightarrow C(\theta)/C(0) \quad (25)$$

with

$$C(\theta) = \sum_\ell \frac{(2\ell + 1)}{4\pi} C_\ell W_\ell^{\text{smooth}} P_\ell^0(\cos \theta). \quad (26)$$

$C_\ell$  is the input power spectrum, and  $W_\ell^{\text{smooth}}$  is the window function which includes all the additional smoothing.

## 2.4 Relation to other topological estimators

The excursion set statistics belongs to a more general class of geometrical estimators, which retain information on the spatial distribution of the non-Gaussian signal. In this respect, it is related to many other commonly used topological estimators. For example, since the distribution of peaks with CMB temperatures above/below a given threshold is a subset of the pixel distribution, there is a direct correspondence between the excursion sets and the peak statistics. In presence of weak non-Gaussianity, it is relatively straightforward to repeat the steps illustrated in the previous section for the peak, rather than the pixel ensemble. In fact, once the one- and two dimensional non-Gaussian PDFs are known (equations 15 and 21), one only needs to impose an extra condition in order to select local maxima, but much of the logic remains the same. Hence, analytic expressions for the number density and for the clustering strength above/below threshold can be obtained for the peak statistics as well. We present a more detailed investigation of the peak clustering statistics, extended to non-Gaussian models, in a forthcoming publication; for an exhaustive treatment of the Gaussian case see instead Bond & Efstathiou (1987).

Similarly, other topological or geometrical estimators which utilize information concerning the morphology of the density structure are also directly related to the excursion set statistics. This is for example the case of the Minkowski functionals (Schmalzing & Gorski 1998; Winitzki & Kosowsky 1998; Banday, Zaroubi & Gorski 2000; Hikage et al. 2006, 2008b; Matsubara 2010); the number density defined in Section 2.3 is effectively the first Minkowski functional (i.e. fraction of total area above the threshold), besides some normalization factors. The genus itself (another Minkowski functional) and its derived statistics (Coles 1988; Gott et al. 1990; Smoot et al. 1994; Colley & Gott 2003; Park 2004; Gott et al. 2007) are also directly related to the excursion sets formalism. This is because the genus, being the number of isolated hot spots minus the number of isolated cold spots, can be obtained from the contours for a given threshold temperature and can be parametrized by the area fraction above the threshold – which is given by equation (13) for the pixel ensemble, in the weak non-Gaussian limit.

## 3 CONSTRAINING NON-GAUSSIANITY WITH THE EXCURSION SET STATISTICS

In this section we present numerical results for the number density and for the clustering strength of pixels above/below

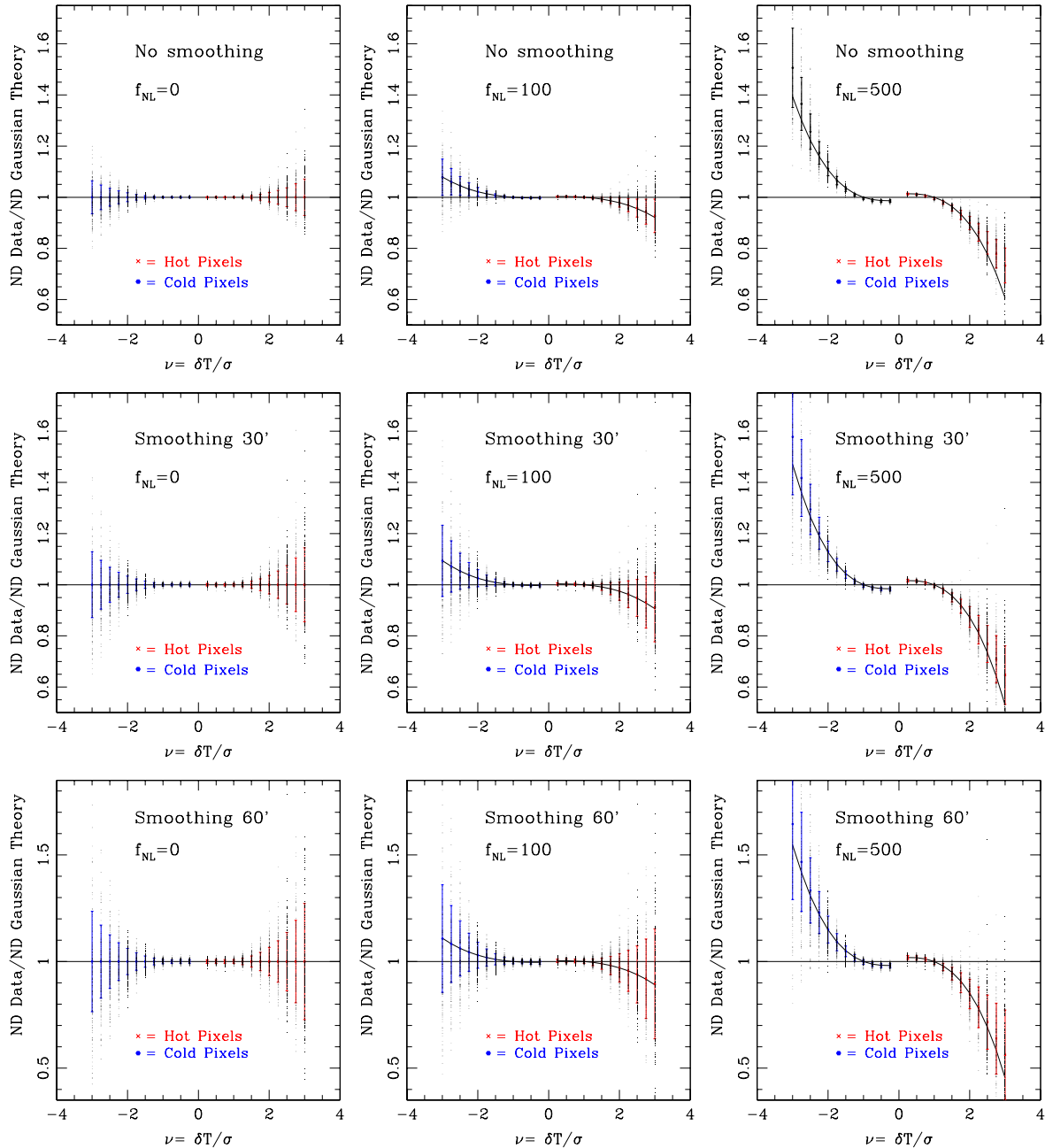


**Figure 3.** Number density of pixels in a Gaussian case (left panels) or in  $f_{\text{NL}}$  models (in the middle panels  $f_{\text{NL}} = 100$ ; in the right ones  $f_{\text{NL}} = 500$ ). A Gaussian smoothing with FWHM=30' and 60' is applied in the central and lower panels, respectively, at  $N_{\text{side}} = 512$ . Errorbars are the  $1\sigma$  run-to-run estimates from 200 maps. Solid curves are theory predictions from equations (12), (13) and (14).

threshold, calculated from non-Gaussian simulations. We also perform a thorough statistical analysis to evaluate the sensitivity of the two observables to the level of non-Gaussianity and to the smoothing resolution. Our calculations are averaged over 200 full-sky CMB realizations, and the associated errorbars are the  $1\sigma$  run-to-run estimates. The effects of noise and of other experimental artifacts, as well as confusion effects due to secondary non-Gaussianities, are not addressed in this analysis; rather, in this first work our main goal is to characterize the intrinsic non-Gaussian CMB signal within the excursion set statistics. However, in

the Appendices B, C and D, we briefly explain how to include these complications in our theoretical framework.

### 3.1 Number density of the excursion set pixels

Figure 3 shows the variation with  $f_{\text{NL}}$  of the pixel number density above (below) threshold, normalized by the expectation from a Gaussian theory (equation 12). No smoothing is applied in all the top panels, while a Gaussian smoothing with FWHM of 30 and 60 arcmin is applied in the intermediate and bottom panels, respectively, at a resolution

$N_{\text{side}} = 512$ . Solid curves are analytic predictions for  $f_{\text{NL}}$  type non-Gaussianity from equations (12-14); they are in very good agreement with our numerical results. Note that due to a relatively small number of maps considered, in practice at higher thresholds the Gaussian mean undergoes a small shift because of statistical fluctuations. We have accounted for this effect in our calculations, and shifted all the corresponding non-Gaussian means by the same amount, as done in Chingangbam & Park (2009). This is the reason why in the figure and in the following ones (4-9) all the Gaussian expectations lie *exactly* on a line. Clearly, this procedure does not affect the relative distance between Gaussian and non-Gaussian means, the quantity we want to characterize here; hence, our results are independent of this small rescaling.

A number of interesting features can be inferred from Figure 3. First, the existence of two regions where the non-Gaussian contribution appears to be more significant, namely at relatively low thresholds ( $\nu = 0.25, 0.50$ ) or around  $\nu = 2.00$ . Second, the fact (never pointed out so far in the literature) that *there are* optimal thresholds which maximize the local non-Gaussianity, as well as others which do not allow for a distinction between the Gaussian and the non-Gaussian case. This is expected from equations (13) and (14); in particular, when  $\nu = 1$  then  $n_{\text{pix}}^{\text{NL}} \equiv 0$  and  $n_{\text{pix}}^{\text{NG}} \equiv n_{\text{pix}}^{\text{G}}$ . Therefore, in this statistical framework levels around  $\nu = 1$  are not sensitive to departures from Gaussianity of the  $f_{\text{NL}}$  local type. Third, at higher thresholds a positive  $f_{\text{NL}}$  causes an enhancement of the number density of the cold pixels and reduces that of the hot ones, while the opposite trend happens when  $\nu < 1$ . This effect is more evident for larger  $f_{\text{NL}}$  values. We will use these findings to devise a new optimal statistical test in the next subsection. An additional Gaussian smoothing increases the errorbars in the number density calculations, and slightly reduces the effect just described.

Figure 4 displays the difference (left panels) and the ratio (right panels) between the number density of hot and cold pixels, at corresponding temperature thresholds, when no smoothing is applied. Top panels highlight the case of  $f_{\text{NL}} = 100$ , bottom panels are for  $f_{\text{NL}} = 500$ . Solid curves show the analytic predictions, which are easily derived from equations (13) and (14). Again, we find a very good agreement between numerical results and analytical expectations. At  $\nu = 1$ , a ‘transition area’ in the number density is clearly visible, particularly when we consider the difference between hot and cold excursion set regions.

### 3.2 Statistical test derived from the number density

The conclusions drawn from Figures 3 and 4 can be expressed in a more quantitative form as follows. If we assume  $n_{\text{pix}}^{\text{NG}}$  to be the possible non-Gaussian discriminator, we can plot the number density measurements in terms of their errorbars. In other words, we can normalize all the points in Figures 3 and 4 by their run-to-run associated errors, and quantify their ‘distance’ from the expected Gaussian predictions. This is quite convenient, as it allows one to re-label which thresholds are particularly sensitive to a local

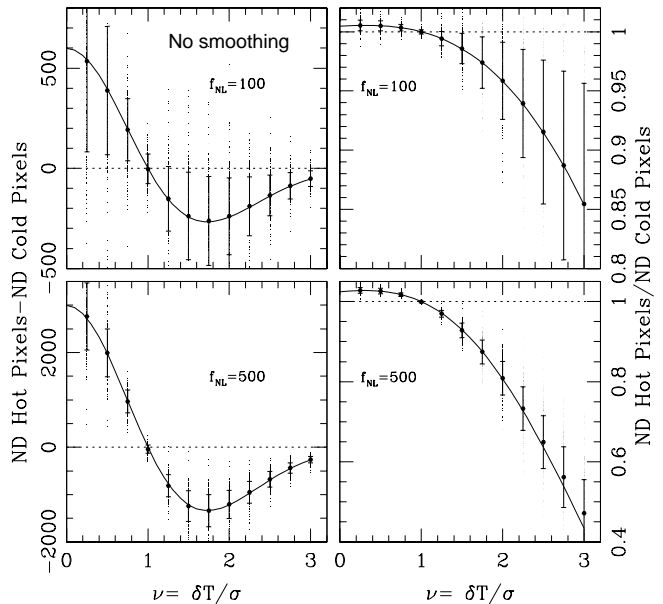


**Figure 4.** Difference (left) and ratio (right) between hot and cold excursion set regions, at corresponding temperature thresholds, when no smoothing is applied. In the top panels  $f_{\text{NL}} = 100$ , in the bottom ones  $f_{\text{NL}} = 500$ . Solid lines are theoretical expectations derived from equations (13) and (14). At  $\nu = 1$ , a transition area in the number density is clearly visible.

non-Gaussian signal, and to determine the exact values of  $\nu$  which maximize departures from Gaussianity.

In Figure 5 we show the case when no smoothing is applied and reinterpret in this context the number density per Gaussian units (left panel), the difference (middle panel) and the ratio (right panel) between the abundance of hot and cold pixels. Shaded areas represent the 1 and 2 $\sigma$  errors, while different symbols are used for different values of  $f_{\text{NL}}$ , as specified in the plots. When  $\nu = 0.25, 0.50$  or  $\nu = 2.00, 2.25$  departures from Gaussianity are maximized: they exceed the 1 $\sigma$  level for  $f_{\text{NL}} = 100$ . Instead, the transition area around  $\nu = 1$  is insensitive to a non-Gaussian signal of the  $f_{\text{NL}}$  type. At higher thresholds, departures are more significant with increasing  $f_{\text{NL}}$ ; however, severe pixel-noise and poor statistics (too few excursion sets) prevent them from being reliable non-Gaussian indicators.

Although the sensitivity of the first skewness parameter  $S^{(0)}$  to  $f_{\text{NL}}$ , and so of the number density itself, is much worse than that of the angular bispectrum (Komatsu & Spergel 2001), the previous findings suggest that we could construct a derived quantity which amplifies the  $f_{\text{NL}}$  contribution. This is achieved by combining two thresholds, where departures from Gaussianity are most significant. Namely,

$$n_{\text{hc}}^{\text{NG}} = n_{\text{hc}}^+ - n_{\text{hc}}^- \quad (27)$$

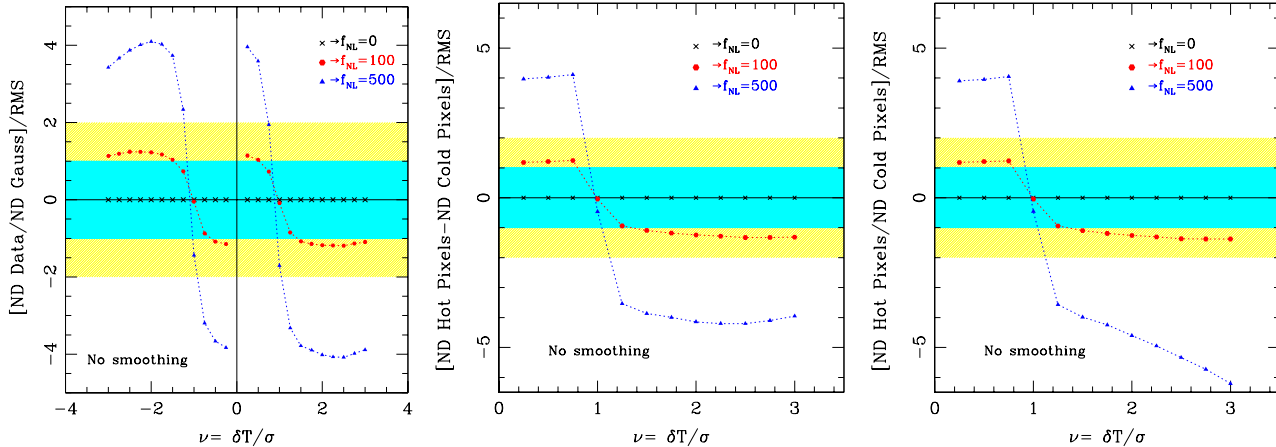
where

$$n_{\text{hc}}^+ = n_{\text{pix}}^{\text{NG}}(\nu = 0.50) - n_{\text{pix}}^{\text{NG}}(\nu = 2.00) \quad (28)$$

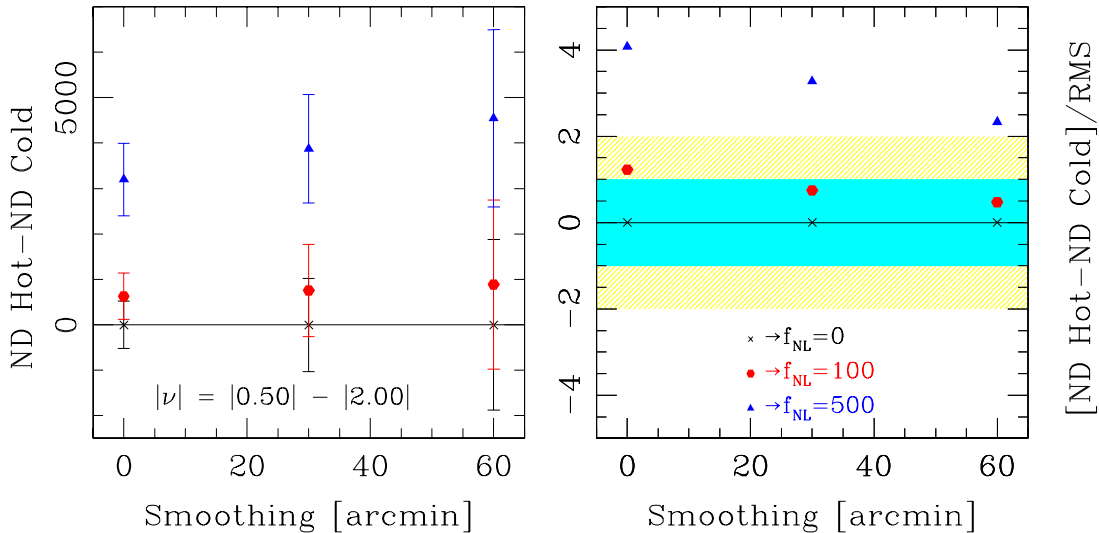
$$n_{\text{hc}}^- = n_{\text{pix}}^{\text{NG}}(\nu = -0.50) - n_{\text{pix}}^{\text{NG}}(\nu = -2.00). \quad (29)$$

Figure 6 shows measurements of this quantity from the simulations, as a function of the smoothing scale adopted. The





**Figure 5.** Reinterpretation of Figure 3 (left panel) and Figure 4 (middle and right panels) in terms of the run-to-run associated errors, in order to quantify the sensitivity of the number density to local non-Gaussianity. Different values of  $f_{\text{NL}}$  are displayed, as indicated in the plots, when no smoothing is applied. Departures from Gaussianity are maximized around  $\nu = 0.25, 0.50$  or around  $\nu = 2.00, 2.25$  while areas close to  $\nu = 1.00$  are insensitive to non-Gaussianity of the local type.



**Figure 6.** Composite quantity for the pixel number density as a function of the smoothing scale, defined by equation (27) in the main text. The left panel is in real units, with errorbars estimated from 200 realizations; the right panel shows similar quantities but in RMS units as in Figure 5. The two areas where the non-Gaussian sensitivity is maximized (i.e.  $|\nu| = 0.50$  and  $|\nu| = 2.00$ ) are combined, in order to boost the departure from Gaussianity.

left panel is real units, the right panel is in errorbar units as in Figure 5. By combining the two optimal levels the sensitivity slightly improves, but still remains at the  $1\sigma$  level for  $f_{\text{NL}} = 100$ . This is because the associated errorbars at different thresholds are correlated.

### 3.3 Clustering strength of the excursion set pixels

Next, we consider the clustering strength of the excursion set regions. We analyze in detail the case of  $\nu = 2.00$ , where according to our previous findings the sensitivity to a local  $f_{\text{NL}}$  type non-Gaussianity is maximized.

Figure 7 shows measurements of the hot and cold pixel

correlations above/below threshold from the simulations. Left panels highlight the Gaussian case, intermediate panels are for  $f_{\text{NL}} = 100$ , and in the right panels  $f_{\text{NL}} = 500$ . A smoothing with FWHM of 30 and 60 arcmin is applied in the central and bottom panels, respectively. Solid lines are analytic predictions in the Gaussian limit, i.e. equation (24).

The various unweighted correlation functions are calculated as explained in Rossi et al. (2009). In particular, the number of random pairs is computed by distributing random points on a unit sphere, and then by pixelizing them in the HEALPix scheme at the same resolution of the maps. The random realization used contains at least 10 times more points than the simulated samples. All the errorbars are es-

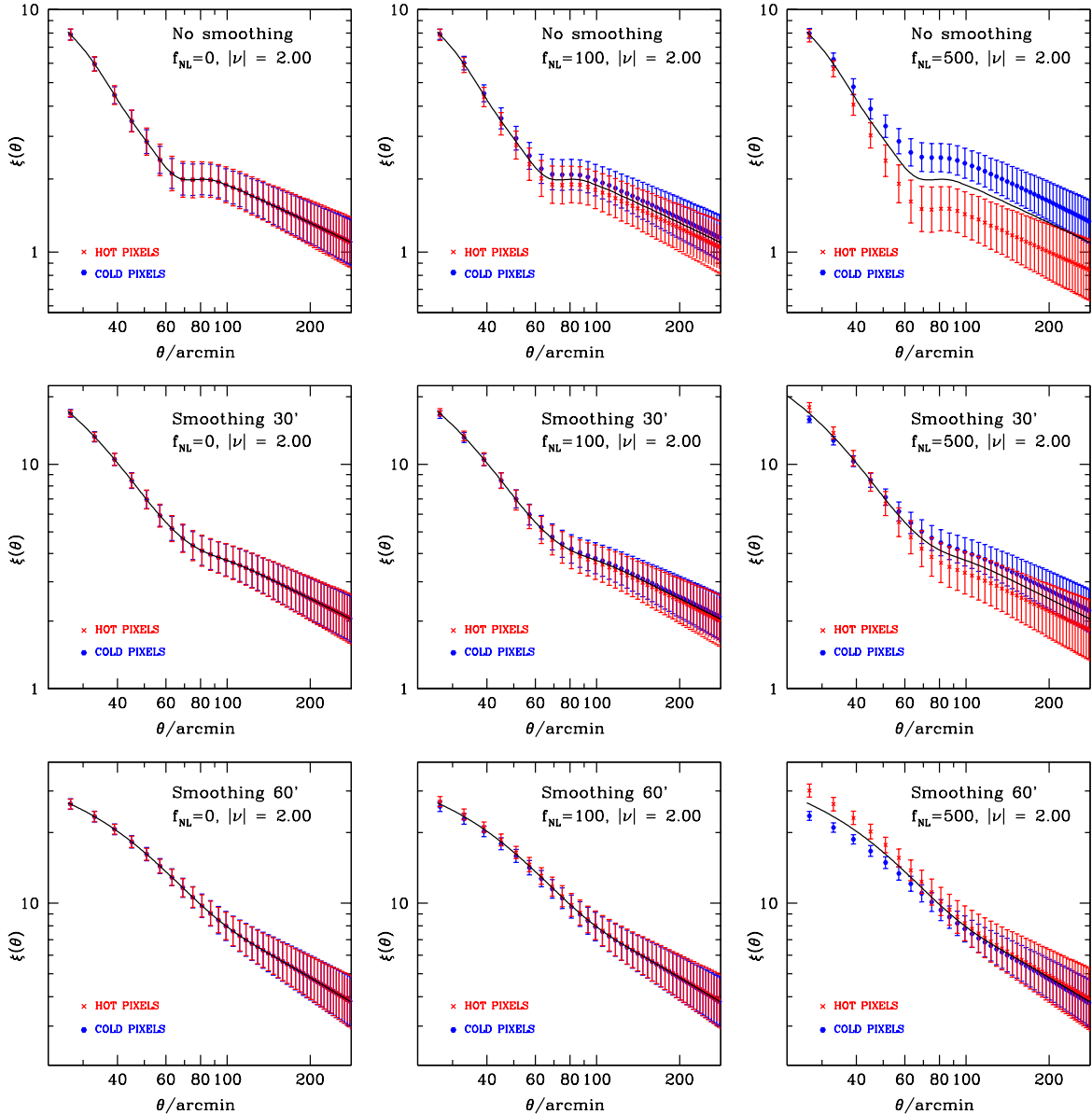


**Figure 7.** Clustering strength of pixels above/below threshold when  $|\nu| = 2.00$ , a regime particularly sensitive to a non-Gaussian signal of the local  $f_{\text{NL}}$  type. Left panels represent the Gaussian case, in the middle panels  $f_{\text{NL}} = 100$ , in the right panels  $f_{\text{NL}} = 500$ . A Gaussian smoothing with FWHM of 30 and 60 arcmin is applied in the middle and bottom panels, respectively. Solid lines are analytic predictions in the Gaussian limit, from equation (24).

timated directly from 200 realizations. Note that the scatter between different runs can be quite significant, especially at relatively large angular scales.

From Figure 7 it is evident that, for a positive and large  $f_{\text{NL}}$  value, the clustering of the cold pixels is enhanced with respect to that of the hot ones. This peculiar feature is a distinct signature of non-Gaussianity of the local  $f_{\text{NL}}$  type. It is most prominent at angular scales of about  $\theta = 75'$ , the Doppler transition due to the sharp turn-down in the power spectrum at  $l \simeq 1500$  (because of the thickness of the last scattering surface). The asymmetry in the excursion set clustering is not surprising: it is expected from the corresponding number density behavior (Figures 3 and 4), and from the shape of the non-Gaussian potential (equation

1). In fact, at thresholds  $\nu > 1$  the cold pixel abundance is amplified with  $f_{\text{NL}}$ , while the number density of the hot pixels is reduced. This causes the difference in the clustering. Also, the quadratic term in (1) is insensitive to a change in sign, hence the asymmetry between hot and cold regions. However, when  $f_{\text{NL}} = 100$  this feature is small, as shown in the middle panels of Figure 7. Therefore, at  $N_{\text{side}} = 512$  the Gaussian correlation function of the excursion sets is not easily distinguishable from a non-Gaussian one, if the model of non-Gaussianity is of the local  $f_{\text{NL}}$  type. Turning the argument around, the excursion set clustering statistic does not provide accurate constraints on Gaussianity itself (at least with this particular non-Gaussian model in mind), contrary to what was previously thought (i.e. Kogut et al.

1995; Barreiro et al. 1998; Heavens & Sheth 1999; Heavens & Gupta 2001). Working at higher resolution would be more advantageous, as at  $N_{\text{side}} = 512$  the predicted error-bars from our simulations are quite large – although they are rather pessimistic estimates, because they are based on 200 runs only. Moreover, smoothing the maps has a more dramatic effect on the clustering of the excursion set regions, rather than on their abundance: the larger-scale power is suppressed, while the small-scale strength is enhanced. This results in an overall suppression of the clustering feature previously described, particularly when  $f_{\text{NL}} = 100$  (see the bottom panels in Figure 7). Note that as we increase the smoothing, the clustering of hot and cold pixels makes a transition between FWHM 30 and 60 arcmin, and the clustering behavior is reversed. At larger smoothing values, we expect the hot pixels to cluster more at larger  $\theta$ . This indicates that large values of FWHM will still be useful for comparison of this quantity with real data. We are addressing this issue in a forthcoming paper, where we deal with the detectability of these non-Gaussian features from a real dataset.

While in Figure 7 solid lines are analytic predictions in the Gaussian limit from equation (24), in Appendix A we show an example of how well the Edgeworth approximation (i.e. equation 21) works for the clustering, when  $f_{\text{NL}} = 100$ . In equation (21), the second and third terms inside the square bracket become important when  $f_{\text{NL}}$  is non-zero. While  $S^{(0)}$  is straightforward to compute, the term  $\lambda$  is much more complicated since it involves the computation of the full-sky three-point function, and it is beyond the scope of this paper. However, we find that ignoring the  $\lambda$  term still gives relatively good agreement with the results from the simulations.

In Figure 8 we show the clustering difference (left panels) and ratio (right panels) between hot and cold excursion set regions, for two significant values of  $f_{\text{NL}}$ . No smoothing is applied. This is done in parallel with the number density case (Figure 4). When  $f_{\text{NL}} = 100$ , the estimated sizes of our errorbars suggest again that a clustering analysis is not ideal to detect departures from Gaussianity, although the behavior at  $f_{\text{NL}} = 500$  is quite peculiar. In the next subsection we propose an optimized statistical test based on the clustering strength, which aims at maximizing the difference between the Gaussian and the non-Gaussian cases.

### 3.4 Statistical test derived from the clustering strength

The conclusions drawn from Figures 7 and 8 can be expressed in a more quantitative form, as was done for the number density in Section 3.2. Assuming now  $\xi_\nu(\theta)$  to be the non-Gaussian discriminator, Figure 9 shows in errorbar units the correlation strength of the excursion set regions per Gaussian expectations (left panel), the difference (middle panel) and the ratio (right panel) between the clustering of hot and cold pixels when  $|\nu| = 2.00$ . No smoothing is applied. Shaded areas represent the 1 and  $2\sigma$  zones, while different symbols are used for different values of  $f_{\text{NL}}$ , as specified in the plots. When  $f_{\text{NL}} = 100$ , departures from Gaussianity lie always below the  $1\sigma$  level, unlike for the abundance case (see Figure 5 for a direct comparison). The situation does not improve significantly if we consider the

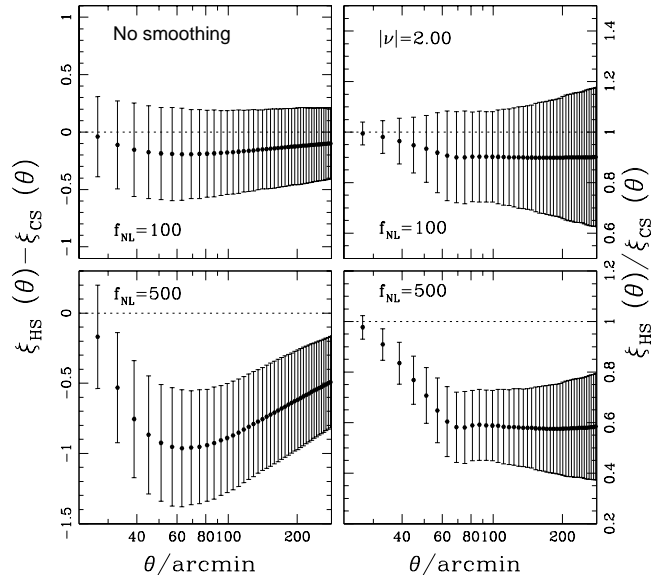


**Figure 8.** Clustering difference (right panels) and ratio (left panels) between hot and cold excursion set regions at  $|\nu| = 2.00$ , when no smoothing is applied. In the top panels  $f_{\text{NL}} = 100$ , in the bottom ones  $f_{\text{NL}} = 500$ . See the main text for more details.

clustering difference or ratio between hot and cold patches. Only when  $f_{\text{NL}} = 500$  there is a noticeable effect, which exceeds  $2\sigma$  around the Doppler scale, at  $\theta \simeq 75$  arcmin.

The scatter in the clustering strength is mainly due to cosmic variance, which causes large fluctuations among different full-sky realizations ( $m$ - and  $\ell$ -modes). As a result, errorbars are large. To minimize its effect, we propose a statistical test, which involves the clustering information alone. The procedure can be summarized as follows.

(i) Consider a non-Gaussian CMB temperature map and extract its power spectrum.

(ii) Use equation (24) to compute the corresponding analytic expectation for the pixel correlations above/below a threshold  $\nu$ , as if the map were thought to be Gaussian. Denote this quantity as  $\xi_{\nu, \text{Gauss}}^{\text{NG}}$ ; it is the same for hot and cold excursion set regions, in the Gaussian statistics.

(iii) Compute the hot and cold correlation functions  $\xi_{\nu, \text{h}}^{\text{NG}}$  and  $\xi_{\nu, \text{c}}^{\text{NG}}$  directly from the map, at the same threshold level.

(iv) Construct the quantities:

$$\xi_{\nu, \text{h}}^{\text{NG}} = (\xi_{\nu, \text{h}}^{\text{NG}} - \xi_{\nu, \text{Gauss}}^{\text{NG}}) / \xi_{\nu, \text{Gauss}}^{\text{NG}} \quad (30)$$

$$\xi_{\nu, \text{c}}^{\text{NG}} = (\xi_{\nu, \text{c}}^{\text{NG}} - \xi_{\nu, \text{Gauss}}^{\text{NG}}) / \xi_{\nu, \text{Gauss}}^{\text{NG}} \quad (31)$$

and plot them as a function of the angular separation  $\theta$ .

(v) Repeat this procedure for the entire set of non-Gaussian maps, with different  $f_{\text{NL}}$  values.

Results of these measurements are shown in the left part of Figure 10;  $f_{\text{NL}} = 100$  in the top panels,  $f_{\text{NL}} = 500$  in the bottom ones. By subtracting the power spectrum contribution in the numerator of (30) and (31), the cosmic variance is partially reduced because fluctuations in the corresponding  $\ell$ -modes are cancelled. Unfortunately, the scatter in the  $m$ -modes is still quite significant, so that at  $f_{\text{NL}} = 100$  it

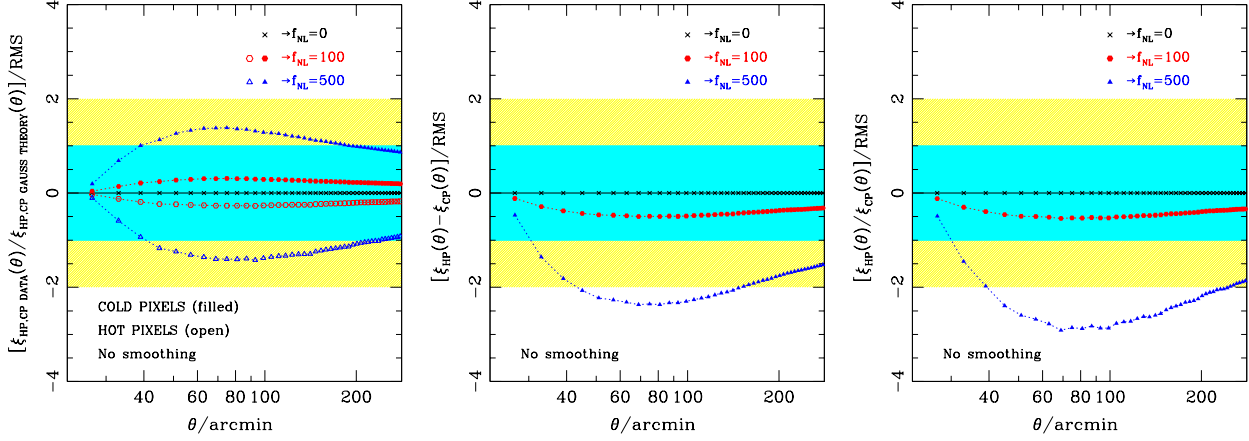


**Figure 9.** Reinterpretation of Figure 7 (left panel) and Figure 8 (middle and right panels) in terms of the run-to-run associated errors, in order to quantify the sensitivity of the excursion set clustering strength to local non-Gaussianity. Different values of  $f_{\text{NL}}$  are displayed, as indicated in the plots, as a function of the angular separation  $\theta$ . No smoothing is applied. Only when  $f_{\text{NL}}$  is of the order of 500 there is a noticeable difference in the clustering, which exceeds the  $2\sigma$  level around the Doppler scale ( $\theta \simeq 75'$ ) when  $|\nu| = 2.00$ .

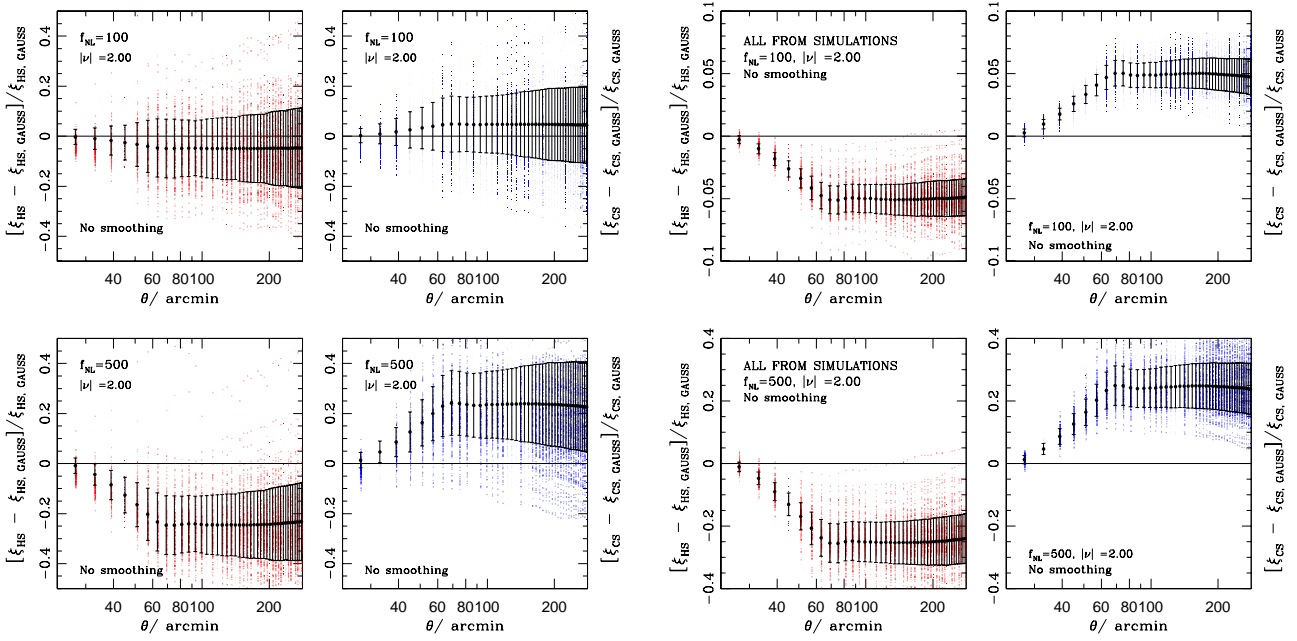


**Figure 10.** Statistical test which involves the clustering information alone, as explained in the main text. [Left] Measurements of the quantities (30) and (31) from the non-Gaussian simulations, with the corresponding Gaussian theoretical prediction  $\xi_{\nu, \text{Gauss}}^{\text{NG}}$  estimated from the same maps. [Right] Same as the left panels, but now  $\xi_{\nu, \text{Gauss}}^{\text{NG}}$  is computed from the corresponding Gaussian maps with the same random seeds of the non-Gaussian ones. In this way, the cosmic variance effect is completely cancelled.

is not possible to distinguish a weakly non-Gaussian signal from a Gaussian one using the clustering information alone.

The idealized situation is presented in the right part of the same figure. Here, we replace  $\xi_{\nu, \text{Gauss}}^{\text{NG}}$  by its direct measurement from the corresponding Gaussian map with the same random seed. In other words, we do not use equation (30) and the non-Gaussian power spectrum to determine  $\xi_{\nu, \text{Gauss}}^{\text{NG}}$ . Instead, we produce a Gaussian map with the same random seed of the non-Gaussian one, and use it to compute the theoretical expectation. This is repeated for

the entire set of non-Gaussian realizations. The procedure is essentially the CMB analogous of what has been proposed by Seljak (2009) for the LSS. In fact, in this way the cosmic variance effect is completely cancelled; even at  $f_{\text{NL}} = 100$ , a clustering analysis would then provide  $\sim 5\%$  difference at the Doppler peak with respect to the Gaussian case.

The situation described here is clearly ideal, because only the first procedure (left panels in Figure 10) can be performed from a real dataset. However, it provides some important insights: cosmic variance is the real limit and ob-

stack within this statistical framework. If we could somehow control the fluctuations in the  $m$ -modes, then the excursion set analysis would provide a powerful tool to detect non-Gaussianity. The problem is that the CMB alone does not allow one to compare ‘tracers’ at different epochs (as for the LSS case), and so to eliminate completely the effect of cosmic variance.

## 4 CONCLUSIONS

We have extended and applied the statistics of the excursion sets to models with primordial non-Gaussianity of the  $f_{\text{NL}}$  local type. While in presence of Gaussian initial conditions many statistics based on geometrical and topological properties of the CMB temperature have been developed and well-studied, to date fewer analyses have been focused on geometrical properties of the CMB radiation in the presence of primordial non-Gaussianity. In particular, our work is the first extension of the excursion set formalism to local  $f_{\text{NL}}$  type non-Gaussianity.

From a large set of simulated full-sky non-Gaussian maps, we computed the number density and the spatial clustering of CMB patches above/below a temperature threshold (Section 3). We found that a positive value of  $f_{\text{NL}}$  enhances the number density of the cold CMB excursion sets (Figures 3, 4) along with their clustering strength (Figures 7, 8) and reduces that of the hot ones.

We performed a thorough statistical analysis to evaluate the sensitivity of the two observables to the level of non-Gaussianity and to the smoothing resolution. We also provided the analytical formalism to interpret our results (Section 2). Expressions for the one- and two-dimensional PDFs (Equations 15 and 21) were obtained from a perturbative approach by the multidimensional Edgeworth expansion around a Gaussian distribution function, and used to characterize the abundance and clustering statistics as a function of  $f_{\text{NL}}$  (Equations 13, 16, 24). We showed that there are optimal thresholds which maximize the local  $f_{\text{NL}}$  non-Gaussianity ( $\nu = 0.25, 0.50$  and  $\nu = 2.00, 2.25$ ), as well as others ( $\nu = 1.00$ ) which do not allow for a distinction between the Gaussian and the non-Gaussian signals (Figures 5 and 9). We devised a new statistical test based of the number density (Section 3.2), which combines two thresholds where departures from Gaussianity are most significant (Figure 6 and Equation 27). We also proposed a new procedure aimed at minimizing the effect of cosmic variance (Section 3.4), which involves the clustering information alone (Figure 10, Equations 30 and 31).

Although we focused here on  $f_{\text{NL}}$  models of the local type, the statistical tools developed are more general and can be applied to describe any other type of non-Gaussianity. A typical example is represented by the curvaton model, for which the cubic term indicated as  $g_{\text{NL}}$  can be large, while  $f_{\text{NL}}$  can be negligible. Our technique can be applied to this case as well, and it is the subject of a forthcoming publication.

This work was primarily motivated by our previous finding (Rossi et al. 2009), namely a remarkable difference in the clustering of hot and cold pixels at relatively small angular scales from the WMAP 5-yr data. We analyzed the possibility that this discrepancy may arise from primordial

non-Gaussianity of the local  $f_{\text{NL}}$  type (Section 3.3), and concluded that only a large value of  $f_{\text{NL}}$  would provide such a difference (Figure 7). Cosmic variance plays a crucial role within this statistical framework, so that the Gaussian correlation function of the excursion sets is not easily distinguishable from the non-Gaussian one, contrary to what was previously thought. In fact, while a distinct signature in the clustering of hot and cold pixels clearly emerges for a large  $f_{\text{NL}}$  non-Gaussianity, particularly at angular scales of about 75 arcmin (around the Doppler peak), as expected this feature is reduced when  $f_{\text{NL}} = 100$ . The clustering behavior is also strongly affected by the smoothing angle. These findings suggest that Gaussianity itself cannot be accurately constrained from the excursion set clustering statistics. In fact, if in principle the use of pixel-pixel correlation functions as a test of Gaussianity is very powerful, because there are no free parameters once the underlying power spectrum has been measured, this may not be the case if the non-Gaussian model is of the  $f_{\text{NL}}$  local type, and  $f_{\text{NL}}$  is small.

Our study was focused on a few selected values of thresholds and two different statistics, so that the predicted constraints on  $f_{\text{NL}}$  are wider than what one would get by combining several threshold levels and different smoothing angles. In this respect, our predicted constraints from the excursion sets are compatible with those of Smidt et al. (2010), obtained from the trispectrum.

Since cosmic variance is the main obstacle in the analysis, we are considering derived statistics which could potentially beat its effect and maximize the non-Gaussian contribution. It is also important to adopt different and complementary statistical approaches, and not just a single view, because there is no such statistics which describes fully and uniquely the non-Gaussian nature of a sample. To this end, a lot of effort has recently gone into developing optimal estimators, and in this sense our statistical technique belongs to a class of topological estimators which may be considered “sub-optimal” for measuring non-Gaussianity. However, in reality all the geometrical methods complement and “diagnose” results obtained with bispectrum or trispectrum estimators. Moreover, geometrical techniques are often model-independent, easy to implement, with low computational cost, and they can retain information on the spatial distribution of the non-Gaussian signal. Also, they provide useful analytic insights and physical intuition. For example, the derivation and implementation of the analytical formula for the CMB Minkowski functionals in the limit of weak non-Gaussianity (Hikage, Komatsu & Matsubara 2006; Matsubara 2010) has allowed to obtain limits on various models, for which the optimal estimators are difficult to implement; at the moment, a limit on the primordial non-Gaussianity in the isocurvature perturbation is available *only* from the Minkowski functionals (Hikage et al. 2009). Note also that the concept of “optimal” is often misleading, as it requires a posteriori knowledge of the type of non-Gaussianity which is, at least in principle, unknown. The main question, instead, is whether or not it is possible to improve limits on  $f_{\text{NL}}$  using the CMB data only.

Including realistic effects in our simulations, such as inhomogeneous noise, point source contamination or foregrounds, so that we can compare our predictions with current observations, is subject of ongoing work (we provide some discussion in Appendices B and D). We present re-

sults of these investigations in a companion paper, where we also consider more terms in the expansion (1). Application of the formalism presented in Section 2.3 to peak rather than pixel statistics is a straightforward exercise, and is also the subject of another forthcoming publication.

The Planck satellite with its increased sensitivity and resolution is expected to improve the measurements of most cosmological parameters by several factors compared to WMAP, and in synergies with future galaxy surveys (Colombo, Pierpaoli & Pritchard 2009). In fact, Planck gains a factor of 2.5 in angular resolution and up to 10 in instantaneous sensitivity with respect to WMAP, and it is nearly photon noise limited in the CMB channels (100-200 GHz). Repeating this analysis at the Planck resolution may then provide more stringent limits on  $f_{\text{NL}}$  from the excursion set statistics, and is also the subject of work in progress.

## ACKNOWLEDGMENTS

We dedicate this paper to the memory of KIAS president Prof. Hyo Chul Myung, who passed away on February 11, 2010. We thank an anonymous referee for helpful comments and suggestions. We acknowledge the support of the Korea Science and Engineering Foundation (KOSEF) through the Astrophysical Research Center for the Structure and Evolution of the Cosmos (ARCSEC). We acknowledge the use of the *Legacy Archive for Microwave Background Data Analysis (LAMBDA)*, support for which is provided by the National Aeronautics and Space Administration (NASA) Office of Space Science. Some of the results in this paper have been derived using the *HEALPix* package (Górski et al. 1999). The computation in the paper was done on the QUEST cluster at KIAS.

## REFERENCES

- Acquaviva, V., Bartolo, N., Matarrese, S., & Riotto, A. 2003, *Nuclear Physics B*, 667, 119
- Adler, R. J. 1981, *The Geometry of Random Fields*, Chichester: Wiley, 1981
- Afshordi, N., & Tolley, A. J. 2008, *Phys. Rev. D*, 78, 123507
- Alishahiha, M., Silverstein, E., & Tong, D. 2004, *Phys. Rev. D*, 70, 123505
- Arkani-Hamed, N., Creminelli, P., Mukohyama, S., & Zaldarriaga, M. 2004, *Journal of Cosmology and Astro-Particle Physics*, 4, 1
- Babich, D., Creminelli, P., & Zaldarriaga, M. 2004, *Journal of Cosmology and Astro-Particle Physics*, 8, 9
- Banday, A. J., Zaroubi, S., & Górski, K. M. 2000, *ApJ*, 533, 575
- Bardeen, J. M., Bond, J. R., Kaiser, N., & Szalay, A. S. 1986, *ApJ*, 304, 15
- Barreiro, R. B., Martínez-González, E., & Sanz, J. L. 2001, *MNRAS*, 322, 411
- Barreiro, R. B., Sanz, J. L., Martínez-González, E., & Silk, J. 1998, *MNRAS*, 296, 693
- Barreiro, R. B., Sanz, J. L., Martínez-González, E., Cayon, L., & Silk, J. 1997, *ApJ*, 478, 1
- Bartolo, N., Matarrese, S., & Riotto, A. 2010, arXiv:1001.3957
- Bartolo, N., & Riotto, A. 2009, *Journal of Cosmology and Astro-Particle Physics*, 3, 17
- Bartolo, N., Matarrese, S., & Riotto, A. 2006, *Journal of Cosmology and Astro-Particle Physics*, 6, 24
- Bartolo, N., Komatsu, E., Matarrese, S., & Riotto, A. 2004, *Phys. Rep.*, 402, 103
- Berry, M. V. 1973, *Royal Society of London Philosophical Transactions Series A*, 273, 611
- Bond, J. R., & Efstathiou, G. 1987, *MNRAS*, 226, 655
- Brandenberger, R. 2009, *Phys. Rev. D*, 80, 023535
- Buchbinder, E. I., Khoury, J., & Ovrut, B. A. 2008, *Physical Review Letters*, 100, 171302
- Cabella, P., Liguori, M., Hansen, F. K., Marinucci, D., Matarrese, S., Moscardini, L., & Vittorio, N. 2005, *MNRAS*, 358, 684
- Carbone, C., Verde, L., & Matarrese, S. 2008, *ApJ*, 684, L1
- Chen, G., & Szapudi, I. 2006, *ApJ*, 647, L87
- Chen, X. 2005, *Phys. Rev. D*, 72, 123518
- Chen, X., Hu, B., Huang, M.-x., Shiu, G., & Wang, Y. 2009, *Journal of Cosmology and Astro-Particle Physics*, 8, 8
- Chen, X., Easther, R., & Lim, E. A. 2008, *Journal of Cosmology and Astro-Particle Physics*, 4, 10
- Chiang, L.-Y., Naselsky, P. D., & Coles, P. 2007, *ApJ*, 664, 8
- Chiang, L.-Y., Naselsky, P. D., Verkhodanov, O. V., & Way, M. J. 2003, *ApJ*, 590, L65
- Chingangbam, P., & Park, C. 2009, *Journal of Cosmology and Astro-Particle Physics*, 12, 19
- Chiu, W. A., Ostriker, J. P., & Strauss, M. A. 1998, *ApJ*, 494, 479
- Chodorowski, M. J., & Bouchet, F. R. 1996, *MNRAS*, 279, 557
- Coles, P. 1988, *MNRAS*, 234, 509
- Coles, P., & Barrow, J. D. 1987, *MNRAS*, 228, 407
- Colley, W. N., & Gott, J. R. 2003, *MNRAS*, 344, 686
- Colombo, L. P. L., Pierpaoli, E., & Pritchard, J. R. 2009, *MNRAS*, 398, 1621
- Copi, C. J., Huterer, D., Schwarz, D. J., & Starkman, G. D. 2007, *Phys. Rev. D*, 75, 023507
- Copi, C. J., Huterer, D., Schwarz, D. J., & Starkman, G. D. 2006, *MNRAS*, 367, 79
- Coulson, D., Ferreira, P., Graham, P., & Turok, N. 1994, *Nature*, 368, 27
- Creminelli, P., Senatore, L., Zaldarriaga, M., & Tegmark, M. 2007, *Journal of Cosmology and Astro-Particle Physics*, 3, 5
- Creminelli, P., & Senatore, L. 2007, *Journal of Cosmology and Astro-Particle Physics*, 11, 10
- Crociani, D., Moscardini, L., Viel, M., & Matarrese, S. 2009, *MNRAS*, 394, 133
- Cruz, M., Martínez-González, E., Vielva, P., Diego, J. M., Hobson, M., & Turok, N. 2008, *MNRAS*, 390, 913
- Cruz, M., Turok, N., Vielva, P., Martínez-González, E., & Hobson, M. 2007, *Science*, 318, 1612
- Cruz, M., Tucci, M., Martínez-González, E., & Vielva, P. 2006, *MNRAS*, 369, 57
- Cruz, M., Martínez-González, E., Vielva, P., & Cayón, L. 2005, *MNRAS*, 356, 29
- Curto, A., Martínez-González, E., Mukherjee, P., Barreiro, R. B., Hansen, F. K., Liguori, M., & Matarrese, S. 2009, *MNRAS*, 393, 615

- Dalal, N., Doré, O., Huterer, D., & Shirokov, A. 2008, *Phys. Rev. D*, 77, 123514
- de Oliveira-Costa, A., Tegmark, M., Zaldarriaga, M., & Hamilton, A. 2004, *Phys. Rev. D*, 69, 063516
- Desjacques, V., & Seljak, U. 2010, *Phys. Rev. D*, 81, 023006
- Desjacques, V., Seljak, U., & Iliev, I. T. 2009, *MNRAS*, 396, 85
- Dvali, G., Gruzinov, A., & Zaldarriaga, M. 2004, *Phys. Rev. D*, 69, 083505
- Eriksen, H. K., Banday, A. J., Górski, K. M., Hansen, F. K., & Lilje, P. B. 2007, *ApJ*, 660, L81
- Eriksen, H. K., Novikov, D. I., Lilje, P. B., Banday, A. J., & Górski, K. M. 2004, *ApJ*, 612, 64
- Gangui, A., Lucchin, F., Matarrese, S., & Mollerach, S. 1994, *ApJ*, 430, 447
- Górski, K. M. et al., 1999, in *Proc. MPA/ESO Conf. "Evolution of Large-Scale Structure: From Recombination to Garching"*
- Gott, J. R., et al. 2008, *ApJ*, 675, 16
- Gott, J. R., Colley, W. N., Park, C.-G., Park, C., & Mugnolo, C. 2007, *MNRAS*, 377, 1668
- Gott, J. R., Park, C., Juszkievicz, R., Bies, W. E., Bennett, D. P., Bouchet, F. R., & Stebbins, A. 1990, *ApJ*, 352, 1
- Grossi, M., Branchini, E., Dolag, K., Matarrese, S., & Moscardini, L. 2008, *MNRAS*, 390, 438
- Gurzadyan, V. G., Starobinsky, A. A., Ghahramanyan, T., Kashin, A. L., Khachatryan, H. G., Kuloghlian, H., Vetrugno, D., & Yegorian, G. 2008, *A&A*, 490, 929
- Hanson, D., Smith, K. M., Challinor, A., & Liguori, M. 2009, *Phys. Rev. D*, 80, 083004
- Heavens, A. F. 1998, *MNRAS*, 299, 805
- Heavens, A. F., & Gupta, S. 2001, *MNRAS*, 324, 960
- Heavens, A. F., & Sheth, R. K. 1999, *MNRAS*, 310, 1062
- Hernández-Monteagudo, C., Kashlinsky, A., & Atrio-Barandela, F. 2004, *A&A*, 413, 833
- Hikage, C., Coles, P., Grossi, M., Moscardini, L., Dolag, K., Branchini, E., & Matarrese, S. 2008, *MNRAS*, 385, 1613
- Hikage, C., Matsubara, T., Coles, P., Liguori, M., Hansen, F. K., & Matarrese, S. 2008, *MNRAS*, 389, 1439
- Hikage, C., Komatsu, E., & Matsubara, T. 2006, *ApJ*, 653, 11
- Hinshaw, G., et al. 1994, *ApJ*, 431, 1
- Hou, Z., Banday, A. J., Górski, K. M., Groeneboom, N. E., & Eriksen, H. K. 2010, *MNRAS*, 401, 2379
- Jensen, L. G., & Szalay, A. S. 1986, *ApJ*, 305, L5
- Jeong, D., & Komatsu, E. 2009, *ApJ*, 703, 1230
- Jones, B. 1996, in *Lineweaver C. H., Bartlett J. G., Blanchard A., Signore M., Silk J., eds, Proc. NATO ASI, The Cosmic Microwave Background*, p. 67
- Kaiser, N. 1984, *ApJ*, 284, L9
- Kamionkowski, M., Verde, L., & Jimenez, R. 2009, *Journal of Cosmology and Astro-Particle Physics*, 1, 10
- Kashlinsky, A., Hernández-Monteagudo, C., & Atrio-Barandela, F. 2001, *ApJ*, 557, L1
- Kim, J., & Naselsky, P. 2010, arXiv:1002.0148
- Knox, L. 1995, *Phys. Rev. D*, 52, 4307
- Kogut, A., Banday, A. J., Bennett, C. L., Gorski, K. M., Hinshaw, G., Smoot, G. F., & Wright, E. L. 1996, *ApJ*, 464, L29
- Kogut, A., Banday, A. J., Bennett, C. L., Hinshaw, G., Lubin, P. M., & Smoot, G. F. 1995, *ApJ*, 439, L29
- Komatsu, E. 2010, *Classical and Quantum Gravity*, 27, 124010
- Komatsu, E., et al. 2010, arXiv:1001.4538
- Komatsu, E., et al. 2009, *ApJS*, 180, 330
- Komatsu, E., et al. 2009, *astro2010: The Astronomy and Astrophysics Decadal Survey*, 2010, 158
- Komatsu, E., Spergel, D. N., & Wandelt, B. D. 2005, *ApJ*, 634, 14
- Komatsu, E., & Spergel, D. N. 2001, *Phys. Rev. D*, 63, 063002
- Kotz, T., Balakrishnan, N., & Johnson, N. L. 2000, *Continuous Multivariate Distributions, Vol. 1, Models and Applications*, John Wiley & Sons, New York
- Koyama, K., Mizuno, S., Vernizzi, F., & Wands, D. 2007, *Journal of Cosmology and Astro-Particle Physics*, 11, 24
- Lam, T. Y., & Sheth, R. K. 2009, *MNRAS*, 398, 2143
- Land, K., & Magueijo, J. 2007, *MNRAS*, 378, 153
- Land, K., & Magueijo, J. 2005, *MNRAS*, 357, 994
- Lehners, J.-L., & Steinhardt, P. J. 2008, *Phys. Rev. D*, 77, 063533
- Liguori, M., Sefusatti, E., Fergusson, J. R., & Shellard, E. P. S. 2010, arXiv:1001.4707
- Liguori, M., Matarrese, S., & Moscardini, L. 2003, *ApJ*, 597, 57
- Linde, A., & Mukhanov, V. 1997, *Phys. Rev. D*, 56, 535
- Lo Verde, M., Miller, A., Shandera, S., & Verde, L. 2008, *Journal of Cosmology and Astro-Particle Physics*, 4, 14
- Lyth, D. H., & Riotto, A. 2006, *Physical Review Letters*, 97, 121301
- Lyth, D. H., Ungarelli, C., & Wands, D. 2003, *Phys. Rev. D*, 67, 023503
- Lyth, D. H., & Wands, D. 2002, *Physics Letters B*, 524, 5
- Maldacena, J. 2003, *Journal of High Energy Physics*, 5, 13
- Mangilli, A., & Verde, L. 2009, *Phys. Rev. D*, 80, 123007
- Matarrese, S., & Verde, L. 2008, *ApJ*, 677, L77
- Matarrese, S., Verde, L., & Jimenez, R. 2000, *ApJ*, 541, 10
- Matsubara, T. 2010, arXiv:1001.2321
- Matsubara, T. 2003, *ApJ*, 584, 1
- Matsubara, T. 1994, *ApJ*, 434, L43
- McDonald, P. 2008, *Phys. Rev. D*, 78, 123519
- Munshi, D., & Heavens, A. 2010, *MNRAS*, 401, 2406
- Naruko, A., & Sasaki, M. 2009, *Progress of Theoretical Physics*, 121, 193
- Naselsky, P., Chiang, L.-Y., Olesen, P., & Novikov, I. 2005, *Phys. Rev. D*, 72, 063512
- Park, C.-G. 2004, *MNRAS*, 349, 313
- Park, C., et al. 2005, *ApJ*, 633, 11
- Park, C., Colley, W. N., Gott, J. R., Ratra, B., Spergel, D. N., & Sugiyama, N. 1998, *ApJ*, 506, 473
- Pietrobon, D., Cabella, P., Balbi, A., de Gasperis, G., & Vittorio, N. 2009, *MNRAS*, 682
- Pillepich, A., Porciani, C., & Hahn, O. 2010, *MNRAS*, 402, 191
- Räth, C., Morfill, G. E., Rossmannith, G., Banday, A. J., & Górski, K. M. 2009, *Physical Review Letters*, 102, 131301
- Rossi, G., Sheth, R. K., Park, C., & Hernández-Monteagudo, C. 2009, *MNRAS*, 399, 304
- Rudjord, Ø., Hansen, F. K., Lan, X., Liguori, M., Marinucci, D., & Matarrese, S. 2009, *ApJ*, 701, 369
- Salopek, D. S., & Bond, J. R. 1990, *Phys. Rev. D*, 42, 3936
- Sasaki, M. 2008, *Progress of Theoretical Physics*, 120, 159
- Sasaki, M., Väiliviita, J., & Wands, D. 2006, *Phys. Rev. D*, 74, 103003

- Schmalzing, J., & Gorski, K. M. 1998, MNRAS, 297, 355  
 Schwarz, D. J., Starkman, G. D., Huterer, D., & Copi, C. J. 2004, Physical Review Letters, 93, 221301  
 Scoccimarro, R. 2000, ApJ, 544, 597  
 Scoccimarro, R., Sefusatti, E., & Zaldarriaga, M. 2004, Phys. Rev. D, 69, 103513  
 Seery, D., & Lidsey, J. E. 2005, Journal of Cosmology and Astro-Particle Physics, 9, 11  
 Sefusatti, E., & Komatsu, E. 2007, Phys. Rev. D, 76, 083004  
 Seljak, U. 2009, Physical Review Letters, 102, 021302  
 Seljak, U., & Zaldarriaga, M. 1996, ApJ, 469, 437  
 Senatore, L., Tassev, S., & Zaldarriaga, M. 2009, Journal of Cosmology and Astro-Particle Physics, 9, 38  
 Slosar, A., Hirata, C., Seljak, U., Ho, S., & Padmanabhan, N. 2008, Journal of Cosmology and Astro-Particle Physics, 8, 31  
 Silvestri, A., & Trodden, M. 2009, Physical Review Letters, 103, 251301  
 Smidt, J., Amblard, A., Cooray, A., Heavens, A., Munshi, D., & Serra, P. 2010, arXiv:1001.5026  
 Smith, K. M., Senatore, L., & Zaldarriaga, M. 2009, Journal of Cosmology and Astro-Particle Physics, 9, 6  
 Smoot, G. F., Tenorio, L., Banday, A. J., Kogut, A., Wright, E. L., Hinshaw, G., & Bennett, C. L. 1994, ApJ, 437, 1  
 Spergel, D. N., et al. 2007, ApJS, 170, 377  
 Taruya, A., Koyama, K., & Matsubara, T. 2008, Phys. Rev. D, 78, 123534  
 Tegmark, M., de Oliveira-Costa, A., & Hamilton, A. J. 2003, Phys. Rev. D, 68, 123523  
 Tojeiro, R., Castro, P. G., Heavens, A. F., & Gupta, S. 2006, MNRAS, 365, 265  
 Verde, L., & Matarrese, S. 2009, ApJ, 706, L91  
 Verde, L., Jimenez, R., Kamionkowski, M., & Matarrese, S. 2001, MNRAS, 325, 412  
 Verde, L., Wang, L., Heavens, A. F., & Kamionkowski, M. 2000, MNRAS, 313, 141  
 Viel, M., Branchini, E., Dolag, K., Grossi, M., Matarrese, S., & Moscardini, L. 2009, MNRAS, 393, 774  
 Vielva, P., & Sanz, J. L. 2009, MNRAS, 397, 837  
 Vielva, P., Wiaux, Y., Martínez-González, E., & Vanderghaynst, P. 2007, MNRAS, 381, 932  
 Yadav, A. P. S., & Wandelt, B. D. 2008, Physical Review Letters, 100, 181301  
 Winitzki, S., & Kosowsky, A. 1998, New Astronomy, 3, 75

## APPENDIX A: ANALYTIC NON-GAUSSIAN PREDICTIONS FOR THE EXCURSION SET PIXEL CLUSTERING

The multidimensional Edgeworth expansion is a convenient way of approximating a PDF in terms of its cumulants. It is a true asymptotic expansion, so that the error is well-controlled; it can be used to describe weak non-Gaussianity.

Figure A1 shows an example of how well the Edgeworth approximation works for the CMB excursion set clustering. Points in the figure are hot and cold pixel correlations above/below a threshold  $|\nu| = 2.00$  from the simulations, when  $f_{\text{NL}} = 100$  and no smoothing is applied. Solid line is the Gaussian analytic prediction from equation (24); dotted

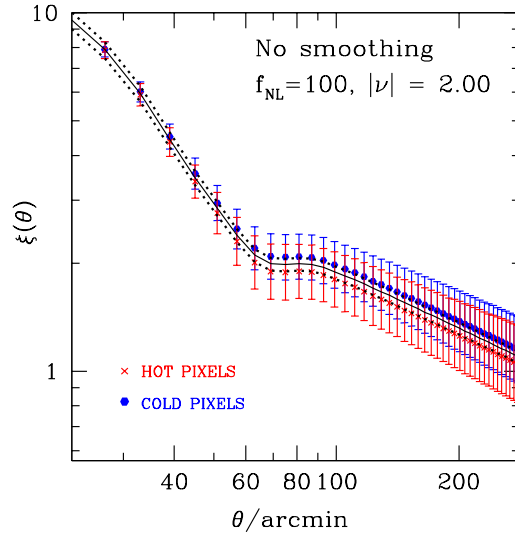


**Figure A1.** Example of how well the Edgeworth approximation works in describing the CMB excursion set clustering when  $f_{\text{NL}} = 100$ . Points are hot and cold pixel correlations above/below  $|\nu| = 2.00$  measured from the simulations, when no smoothing is applied. Solid line is the Gaussian analytic prediction (equation 24). Dotted lines are the non-Gaussian analytic expectations obtained by using equation (21) and by ignoring the  $\lambda$  term. The agreement between numerical results and theory predictions is reasonably good only at large angular scales  $\theta$ .

lines are the non-Gaussian analytic expectations obtained by using equation (21) in (18) and (16), and by ignoring the  $\lambda$  term. The agreement between numerical results and theory predictions is still good at large angular scales  $\theta$ . However, for small values of  $\theta$  we expect  $\lambda \rightarrow \sigma S^{(0)}$ , hence this term becomes important in (21); this is why in Figure A1 the analytic prediction fits poorly in that regime. On the opposite, at higher threshold levels and when  $\sigma S^{(0)}$  becomes large the Edgeworth expansion cannot be used.

## APPENDIX B: INHOMOGENEOUS NOISE AND PARTIAL SKY COVERAGE

The number density and the correlation strength of pixels above/below a temperature threshold  $\nu$  can be generically expressed by

$$n_{\text{pix}}(\nu) = \frac{N_{\text{pix,tot}}}{4\pi} \cdot P_1, \quad (\text{B1})$$

$$1 + \xi_\nu(\theta) = P_2/P_1^2, \quad (\text{B2})$$

where  $N_{\text{pix,tot}}$  is the total number of pixels, and  $P_1$  and  $P_2$  are defined in equations (17) and (18). By inserting the corresponding one- and two-dimensional PDFs in those equations, and by using their output in (B1) and (B2), one can readily characterize the pixel number density and the clustering statistics above/below threshold in the fully Gaussian case or the weak non-Gaussian limit (equations 12–24).

The analytic expressions derived in the main text apply to full-sky intrinsic CMB signal; the effect of noise is not included. However, with the formalism introduced by Rossi et al. (2009) we can also describe analytically the excursion



set clustering in the weak non-Gaussian limit, in presence of inhomogeneous noise. Maintaining the same notation, we indicate the observed value in a pixel by  $D = T - \langle T \rangle \equiv \delta T = s + n$ , which is the sum of the true signal  $s$  plus noise  $n$ , both of which have mean zero. We consider a model in which the signal is homogeneous and may have spatial correlations whereas the noise, independent of the signal, may be inhomogeneous and have spatial correlations. We denote  $p(D)$  the observed one-point distribution of  $D$ ,  $p(s)$  the distribution of  $s$  with rms  $\sigma_S$ ,  $p(\sigma_n)$  the distribution of the rms value of the noise in a pixel, and  $p(n|\sigma_n)$  the distribution of the noise when the rms value of the noise is  $\sigma_n$ . The one-point observed distribution is

$$\begin{aligned} p(D) &= \int ds p(s) \int dn p(n) \delta_D(s + n = D) \\ &= \int ds p(s) \int dn \int d\sigma_n p(n|\sigma_n) p(\sigma_n) \\ &\quad \times \delta_D(s + n = D) \\ &= \int d\sigma_n p(\sigma_n) \int ds p(s) p(D - s|\sigma_n) \\ &= \int d\sigma_n p(\sigma_n) p(D|\sigma_n), \end{aligned} \quad (\text{B3})$$

where  $\delta_D$  is the Dirac delta. The fraction of pixels above some temperature threshold  $D_t$  is

$$\begin{aligned} f(D_t) &= \int_{D_t}^{\infty} dD p(D) = \int d\sigma_n p(\sigma_n) \int_{D_t}^{\infty} dD p(D|\sigma_n) \\ &= \int d\sigma_n p(\sigma_n) f(D_t|\sigma_n). \end{aligned} \quad (\text{B4})$$

Similarly, for two pixels separated by the angular distance  $\theta$ , or having correlation  $w \equiv w(\theta)$ , the two-point observed distribution is specified by:

$$\begin{aligned} p(D_1, D_2, w) &= \int ds_1 \int ds_2 p(s_1, s_2, w) \int dn_1 \int dn_2 \\ &\quad \times p(n_1, n_2) \delta_D(s_1 + n_1 = D_1) \delta_D(s_2 + n_2 = D_2) \\ &= \int ds_1 \int ds_2 p(s_1, s_2, w) \int dn_1 \int dn_2 \int d\sigma_1 \\ &\quad \times \int d\sigma_2 p(n_1, n_2|\sigma_1, \sigma_2) p(\sigma_1, \sigma_2, w) \delta_D(s_1 + n_1 = D_1) \\ &\quad \times \delta_D(s_2 + n_2 = D_2) \\ &= \int d\sigma_1 \int d\sigma_2 p(\sigma_1, \sigma_2, w) \int ds_1 \int ds_2 p(s_1, s_2, w) \\ &\quad \times p(D_1 - s_1|\sigma_1) p(D_2 - s_2|\sigma_2) \\ &= \int d\sigma_1 \int d\sigma_2 p(\sigma_1, \sigma_2, w) p(D_1, D_2, w|\sigma_1, \sigma_2) \end{aligned} \quad (\text{B5})$$

where

$$\begin{aligned} p(D_1, D_2, w|\sigma_1, \sigma_2) &= \int ds_1 \int ds_2 p(s_1, s_2, w) \\ &\quad \times p(D_1 - s_1|\sigma_1) p(D_2 - s_2|\sigma_2). \end{aligned} \quad (\text{B6})$$

Since  $\mu = \delta T/\sigma \equiv s/\sigma_S$ , where  $\mu$  is the variable used in the main text to indicate the threshold level, then  $p(s)ds \equiv p(\mu)d\mu$  and  $p(s_1, s_2, w)ds_1ds_2 \equiv p(\mu_1, \mu_2, w)d\mu_1d\mu_2$ . Therefore we can use the PDFs (15) and (21) to characterize (B3), (B4) and (B5) in the weak non-Gaussian limit, when inhomogeneous noise is present. Once (B3), (B4) and (B5) are

known, then the pixel number density and the clustering above/below threshold can be inferred from (B1) and (B2), where now

$$P_1 = \int_{D_t}^{\infty} p(D)dD \equiv f(D_t) \quad (\text{B7})$$

and

$$P_2 = \int_{D_t}^{\infty} dD_1 \int_{D_t}^{\infty} dD_2 p(D_1, D_2, w). \quad (\text{B8})$$

The corresponding Gaussian limiting case has been presented in detail in Rossi et al. (2009). In particular, if  $p(s_1, s_2, w)$  is bivariate Gaussian with  $\langle s_1^2 \rangle = \langle s_2^2 \rangle = \sigma_S^2$ ,  $\langle s_1 s_2 \rangle = C_S(\theta)$  as defined in equation (26), and the noise  $p(n|\sigma_n)$  is Gaussian with variable rms  $\sigma_n$ , then

$$\begin{aligned} p(D_1, D_2, w|\sigma_1, \sigma_2) &= \frac{1}{2\pi\sqrt{\|C\|}} e^{-\frac{1}{2}D^T \cdot C^{-1} \cdot D} \\ &= \frac{1}{2\pi\sigma_D^2\sqrt{\alpha_1\alpha_2 - w^2}} \exp\left\{-\frac{\alpha_2 D_1^2 + \alpha_1 D_2^2 - 2w D_1 D_2}{2\sigma_D^2(\alpha_1\alpha_2 - w^2)}\right\} \end{aligned} \quad (\text{B9})$$

with  $\alpha_1 = (\sigma_S^2 + \sigma_1^2)/\sigma_D^2$ ,  $\alpha_2 = (\sigma_S^2 + \sigma_2^2)/\sigma_D^2$ , and

$$w = \frac{C_S(\theta) + C_N(\theta)}{\sigma_D^2}, \quad (\text{B10})$$

$$C_N(\theta) = \sum_{\ell} \frac{(2\ell + 1)}{4\pi} C_{\ell}^N W_{\ell}^{\text{smooth}} P_{\ell}^0(\cos \theta), \quad (\text{B11})$$

where  $C$  is the covariance matrix of the temperature field,  $\sigma_D^2$  the variance of  $D$ ,  $C_{\ell}^N$  the power spectrum of the noise map, and  $W_{\ell}^{\text{smooth}}$  the additional smoothing due to finite pixel size, optional Gaussian beam smoothing and mask influence. Note in fact that in presence of incomplete sky coverage one needs to add an extra window function in (26) and in (B11), according to the geometry of the survey, to account for extra-correlations introduced by the mask. If the noise is spatially uncorrelated, then clearly  $C_N(\theta) = 0$  and therefore  $w \equiv C_S(\theta)/\sigma_D^2$ . In the approximation where  $\sigma_1 = \sigma_2$ , rms noise varies spatially on scales much larger than those of interest, then  $\alpha_1 = \alpha_2$ . The ‘‘standard’’ approximation, rms noise independent of position, has  $\alpha_1 = \alpha_2 = 1$ .

Properly characterizing all these experimental complications, when primordial non-Gaussianity is assumed, is the next step in our analysis; it will be presented in a forthcoming publication. In particular, in order to compute (B3), (B4) and (B5) in the weak non-Gaussian limit, a detailed knowledge of the noise distributions is required; namely,  $p(\sigma_n)$ ,  $p(n|\sigma_n)$  and their corresponding two-dimensional expressions must be specified. For example, those PDFs can be directly measured from a real dataset and/or given by the specifics of the experiment (i.e. WMAP, Planck, etc.), as was the case in Rossi et al. (2009).

However, it is straightforward to predict what happens in the presence of Gaussian white noise (independent of position, with rms  $\sigma_N$ ). In fact, in this case the effective rms of the CMB map increases; it is given by  $\sigma \equiv \sigma_D = \sqrt{\sigma_S^2 + \sigma_N^2}$ . Hence, there will be a slight shift in the threshold level  $\nu = D/\sigma_D$ , but all the equations derived in the main text are still applicable – provided that one replaces  $\sigma_S$  with the effective rms of the map,  $\sigma_D$ . Handling inhomogeneous noise is more complicated and will be presented separately, as the

overall effect on the pixel number density and clustering critically depends on the detailed characteristics of the noise.

### APPENDIX C: ANALYTIC ERROR ESTIMATES

For a Gaussian random field, the uncertainties in the pixel number density and in the correlation function above/below threshold can be evaluated analytically from the optimal variance limit, which contains cosmic variance, instrumental noise, and finite bin size effects. Details can be found in Rossi et al. (2009). In essence, the ultimate accuracy with which the CMB power spectrum can be determined at each  $\ell$  is given by (Knox 1995):

$$\Delta C_\ell = \sqrt{\frac{2}{(2\ell+1)f_{\text{sky}}}} \left[ C_\ell + \frac{4\pi\sigma_{\text{N}}^2}{N_{\text{pix,tot}}W_\ell^{\text{instr}}} \right] \quad (\text{C1})$$

where  $W_\ell^{\text{instr}}$  is the instrumental window function and  $f_{\text{sky}}$  the fraction of the sky covered by the experiment. The uncertainty in the angular correlation function for narrow bins in  $\theta$  is then:

$$\begin{aligned} \Delta C(\theta) &= \left\{ \sum_\ell \left| \frac{\partial C(\theta)}{\partial C_\ell} \right|^2 \Delta C_\ell^2 \right\}^{1/2} \\ &= \left\{ \sum_\ell \frac{(2\ell+1)}{8\pi^2 f_{\text{sky}}} |P_\ell^0(\cos\theta)|^2 (W_\ell^{\text{instr}} \cdot W_\ell^{\text{smooth}})^2 \times \right. \\ &\quad \left. \times \left[ \frac{2\pi C_\ell^*}{\ell(\ell+1)} + \frac{\Omega_{\text{pix}}\sigma_{\text{N}}^2}{W_\ell^{\text{instr}}} \right]^2 \right\}^{1/2} \quad (\text{C2}) \end{aligned}$$

where  $C_\ell^* = \ell(\ell+1)C_\ell/2\pi$  and  $\Omega_{\text{pix}} = \theta_{\text{pix}}^2$  is the pixel area. If the bin size is not infinitesimal, one needs to make a small correction – which is negligible for the scales we are interested in (see Rossi et al. 2009 for more details). The uncertainties in the correlation function above/below threshold are finally derived from:

$$\Delta \xi_\nu(\theta) = \left| \frac{\partial \xi_\nu(\theta)}{\partial C(\theta)} \right| \Delta C(\theta). \quad (\text{C3})$$

An example of how well this analytic relation works in the Gaussian limit is shown in Figure C1 by the shaded area. The result is compared with numerical estimates (errorbars), when the full-sky intrinsic CMB signal is considered, in absence of pixel noise. As evident from the figure, the agreement between theoretical expectations from equation (C3) and numerical predictions is good.

In presence of primordial local non-Gaussianity, the situation is more complicated. In principle, one can still follow the previous steps and derive similar analytic expressions. However, when  $f_{\text{NL}} \neq 0$  the power spectrum  $C_\ell$  is different from the Gaussian case, and the full-sky two-point angular correlation function  $C(\theta)$  cannot be expressed as simply as in (26); one needs to account for extra correlations introduced by the primordial non-Gaussianity. If noise is also included, the situation is even more complicated – as presented in Appendix B. If we instead neglect all the contribution from bispectrum to modify the power spectrum and the angular correlation function as for large  $f_{\text{NL}}$ , then (C3) will have an additional term proportional to  $f_{\text{NL}}$ ; the extra non-Gaussian part can be inferred from the two-dimensional PDF (21), i.e. a term proportional to

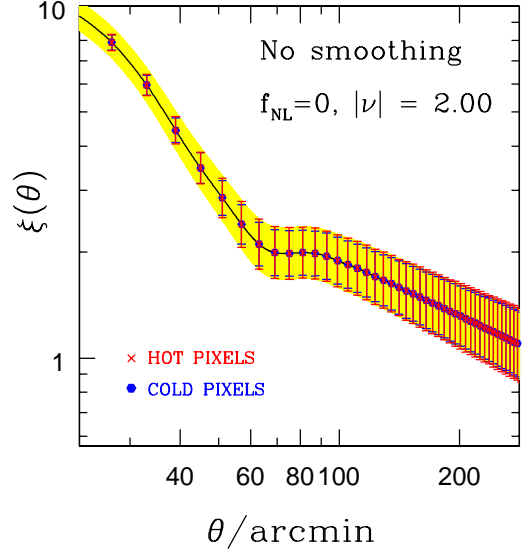


**Figure C1.** Analytic estimate of the errors for the pixel correlation function above/below threshold (shaded area) derived from equation (C3), in the Gaussian limit. Numerical errorbars are also shown; they are in good agreement with the theoretical predictions. The threshold level is  $|\nu| = 2.00$ .

$$\propto S^{(0)} \left( \frac{H_{30} + H_{03}}{6} \right) + O(f_{\text{NL}}). \quad (\text{C4})$$

However, we feel that estimating the errorbars by using a large set of simulations is more accurate, for any arbitrary value of non-Gaussianity and in particular when  $f_{\text{NL}}$  is small. This is why we do not attempt to derive analytic uncertainties in the weak non-Gaussian limit; rather, our approach is to estimate errors using a large set of numerical simulations, with some guidance provided by the analytic expressions (C1-C3) valid in the Gaussian regime.

### APPENDIX D: SPURIOUS NON-GAUSSIANITIES

Even for standard “optimal” estimators like the bispectrum or trispectrum, the problem of non-Gaussianities arising from non-primordial sources is very challenging. There are many different contaminants which can be confused as primordial non-Gaussian signals. Those include (1) *instrumental effects*, such as beam asymmetries, inhomogeneous noise, masks or incomplete sky coverage, (2) *astrophysical contaminants*, such as point sources, foregrounds, presence of voids or anomalous cold spots, (3) *secondary anisotropies*, such as the Integrated Sachs-Wolfe effect (ISW) and lensing, and so forth. In certain cases the contamination is negligible, in other cases it may be severe but one can account for it. There are also situations in which the spurious non-Gaussianity is hard to account for, or its contribution remains still unclear.

Regarding instrumental effects, the inhomogeneity of the noise is the most critical problem. However, in Appendix B we showed how to extend our formalism in presence of inhomogeneous noise. Given a good knowledge of the experimental beams, window functions and noise absolute calibration, it is possible to separate its contribution from a

primordial non-Gaussianity. Another possible contaminant is introduced by partial sky coverage: for instance, edge effects due to pixels which lie very close to the mask could potentially induce undesirable non-Gaussianities, but their effect can be carefully modelled.

As far as astrophysical contaminants, the presence of low-density regions in the southern Galactic cap (cold spots), and the contribution by unknown point sources or anomalous foreground emissions, are all possible sources of confusion. Their accurate measurement is therefore crucial. In particular, uncertainties in the foreground template model used for the foreground subtractions may introduce anomalies at the percentage level, since Galactic foregrounds are non-Gaussian and anisotropic. While an optimal estimator has a clear framework to assess the amount of contribution from secondary sources, in our case we may account for point source contaminations in two ways: theoretically, and by using simulations. For example, from a theoretical point of view, the following calculation shows how to quantify for the contamination in the correlation function. Denote with the subscripts  $P$  a point source, and with  $T$  the pixel temperature; use  $N$  for the respective number of pairs. Assume no correlations between point sources (i.e.  $\xi_{PP} = 0$ ) and neglect possible cross-correlations (i.e.  $\xi_{TP} = 0$ ). The overall observed unweighted correlation function is then:

$$\begin{aligned}
1 + \xi_{\text{obs}} &= \frac{\sum_i w_i (1 + \xi_i)}{\sum_i w_i} \\
&= \frac{N_{TT}(1 + \xi_{TT}) + N_{PP}(1 + \xi_{PP}) + N_{TP}(1 + \xi_{TP})}{N_{TT} + N_{PP} + N_{TP}} \\
&\simeq \frac{N_{TT}(1 + \xi_{TT}) + N_{PP} + N_{TP}}{N_{TT} + N_{PP} + N_{TP}} \\
&= \frac{N_{TT}(1 + \xi_{TT})}{N_{TT} + N_{PP} + N_{TP}} + \frac{N_{PP} + N_{TP}}{N_{TT} + N_{PP} + N_{TP}} \\
&\simeq \frac{N_{TT}(1 + \xi_{TT})}{N_{TT} + N_{PP} + N_{TP}} \tag{D1}
\end{aligned}$$

since  $N_{TT} \gg N_{PP} + N_{TP}$ . Therefore one can write:

$$1 + \xi_{\text{obs}} \simeq \gamma(1 + \xi_{TT}) \tag{D2}$$

where

$$\gamma = \frac{N_{TT}}{N_{TT} + N_{PP} + N_{TP}} \tag{D3}$$

and  $N_{TT} = n_T(n_T - 1)/2$ ,  $N_{PP} = n_P(n_P - 1)/2$ ,  $N_{TP} = n_T n_P$ , with  $n_T$  the number of effective temperature pixels and  $n_P$  the number of spurious undetected point sources (equivalent to bad pixels). With a simulation approach, we can also quantify very accurately the contamination induced by point sources. This is achieved by adding point sources to the mock maps, and by repeating the same analysis as for the uncontaminated case. A comparison between the two situations allows one to quantify the degree of contamination.

Spurious non-Gaussianities could also arise from secondary anisotropies, such as gravitational lensing, cosmic reionization, Sunyaev-Zel'dovich, Sachs-Wolfe or Ostriker-Vishniac effects (see Komatsu 2010 for a recent review). Phase transitions in the early Universe may also introduce a new source of non-Gaussianity, difficult to disentangle from a primordial non-Gaussian signal. In particular, the most serious contamination of the local  $f_{\text{NL}}$  model is represented by the coupling between the ISW and the weak gravitational

lensing: in fact, the coupling between small and large scales creates a local form bispectrum of non-primordial origin. Recently, Hanson et al. (2009) have shown that the lensing-ISW coupling can cause a bias in the  $f_{\text{NL}}$  parameter on the order of  $\Delta f_{\text{NL}} \simeq 10$ . However, in general the primordial non-Gaussian signal can be separated from non-Gaussian secondary anisotropies on scales relevant for WMAP and Planck.

All these effects are of course very important, before one can claim a pure detection of a primordial non-Gaussianity. We are planning to address all these issues in detail, when we apply our techniques to a real dataset.